

# Measurement of CP violation in the analysis of $B^0 \rightarrow J/\psi K_S$ decays with the 2010 LHCb data.

---

MSc thesis

Hartger Weits

Januari 2012

## Abstract

This thesis describes a measurement of the time dependent decay rate asymmetry in  $B^0 \rightarrow J/\psi K_S$  decays with the 2010 LHCb data sample. The found value for  $S$  is  $0.881_{-0.301}^{+0.334}$ , which is compatible with the current world average. A Monte Carlo study has been performed to investigate the lifetime resolution model. Furthermore two Goodness-of-Fit tests applied to the analysis gave a statistical significance of  $p = 0.477$  and  $p = 0.812$ .

UNIVERSITEIT TWENTE.



*Author*  
Hartger Weits

*Committee*  
dr. W. Hulsbergen (supervisor)  
prof. dr. ing. B. van Eijk  
dr. ir. H. Wormeester

**UNIVERSITEIT TWENTE.**

**University of Twente**  
Enschede, The Netherlands

Faculty of Science and Technology  
High Energy Physics chair



**Nikhef**  
National Institute for Subatomic Physics  
Amsterdam, The Netherlands

**LHCb group**

# Contents

<b>Contents</b>	<b>1</b>
<b>1 Introduction</b>	<b>3</b>
1.1 Outline of thesis . . . . .	4
<b>2 B meson analysis</b>	<b>7</b>
2.1 The CKM matrix . . . . .	8
2.2 Mixing . . . . .	9
2.3 Decay rate asymmetry . . . . .	11
2.4 $B^0 \rightarrow J/\psi K_S$ . . . . .	14
<b>3 LHCb detector and data set</b>	<b>17</b>
3.1 Flavour tagging . . . . .	19
3.2 Reconstruction software. . . . .	21
<b>4 Description of the used model</b>	<b>25</b>
4.1 Extended likelihood fit . . . . .	25
4.2 Parametrization . . . . .	26
<b>5 Calibration of the resolution model</b>	<b>29</b>
5.1 Parametrization . . . . .	30
5.2 Dilution . . . . .	32
5.3 Monte Carlo study. . . . .	32
<b>6 Validation of the fit.</b>	<b>37</b>
<b>7 Fit to 2010 data</b>	<b>41</b>
7.1 Systematic errors . . . . .	45
<b>8 Goodness-of-Fit</b>	<b>47</b>
8.1 Distance to Nearest Neighbor . . . . .	48
8.2 Local-Density Method . . . . .	50

<b>9 Conclusion &amp; Outlook</b>	<b>53</b>
<b>A Uniformity of <math>U</math></b>	<b>55</b>
<b>B Pull Distributions</b>	<b>57</b>
<b>C Resolution model dependencies</b>	<b>63</b>
<b>Bibliography</b>	<b>67</b>

# Introduction

Particle physics tries to answer the question what our world is fundamentally made of. In the current view everything around us is a big ocean of tiny particles which are interconnected through four fundamental forces, namely gravity, electromagnetism and the weak and strong nuclear forces.

All matter is made out of 17 different elementary particles: 6 leptons, 6 quarks, and 5 bosons<sup>1</sup>. They are schematically shown in figure 4 together with their interactions. The model which describes the interactions that these particles undergo is called the Standard Model. It is a local Lagrangian field theory that describes the electromagnetic, weak and strong nuclear interactions [14].

Because gravity is not incorporated we know that the Standard Model is not a complete picture. But since its finalization in the mid 1970s it has withstood considerable experimental testing and accurately predicted the existence and properties of new particles that were not yet observed. Among others, it predicted the Z and W boson particles, which were first observed at the UA1 and UA2 experiments at CERN in 1983.

One of the big puzzles in particles physics is the question why there is such a big asymmetry in matter and anti-matter. The whole visible universe seems to be dominated by matter. To generate the current matter abundance, one of the requirements is that the combined symmetry of charge conjugation and space inversion, called CP, must be violated.

The LHCb experiment is one of the four main experiments situated at the Large Hadron Collider at CERN, which is depicted in figure 1.2. Its main purpose is to study this before mentioned CP-violation and weak interactions in the B-meson system, and to measure the branching ratios of rare B-decays.

---

<sup>1</sup>Technically there are 51 different particles when counting antiparticles and color charge.

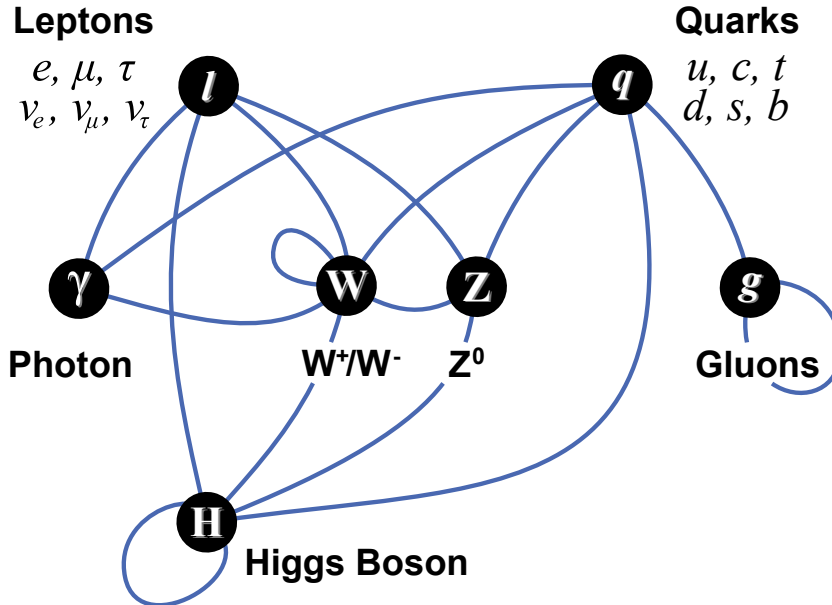


Figure 1.1: Quarks carry electric charge, weak isospin, and color charge. Because of this they interact respectively through the electromagnetic, the weak nuclear force, and the strong nuclear force. The leptons don't carry any color charge. Furthermore the three neutrinos do not carry electric charge either, so their motion is directly influenced only by the weak nuclear force, which makes them difficult to detect. The W and Z bosons are the force carriers for the weak interaction, photons for the electromagnetic, and gluons for the strong interaction. The Higgs boson plays a unique role in the Standard Model, by explaining why the other elementary particles, except the photon and gluon, are massive. The illustrious Higgs boson has not been observed yet, at least at the moment of writing.

One of the decays that LHCb measures is  $B^0 \rightarrow J/\psi K_S$ . This channel is often named the gold-plated mode for the measurement of time-dependent CP violation in the  $B^0$  system. It has a relatively large branching fraction and readily accessible final states with small backgrounds and is theoretically clean. My analysis on CP violation will be done by investigating these decays.

## 1.1 Outline of thesis

The starting point of this analysis, chapter 2, will give a brief overview of the formalism to describe CP violation in  $B^0 \rightarrow J/\psi K_S$  decays in the Standard Model.

In chapter 3 a short outline of the LHCb detector measured these decays is

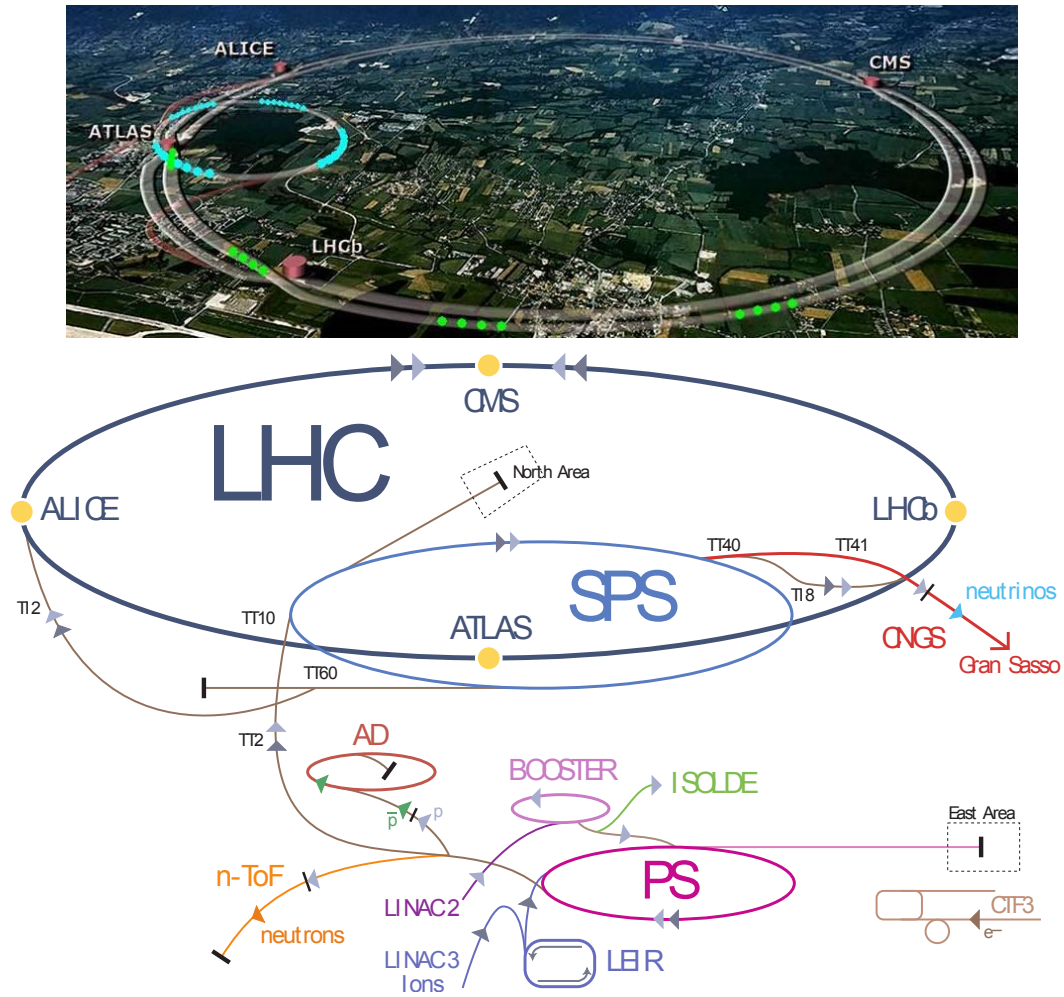


Figure 1.2: The Large Hadron Collider is the world's largest and highest-energy particle accelerator. The LHC lies in a tunnel 27 kilometers in circumference, as deep as 175 metres beneath the Franco-Swiss border near Geneva, Switzerland. This synchrotron is designed to collide opposing particle beams of either protons at an energy of 7 TeV

given. Also the used reconstruction and simulation software is described.

To extract the relevant physical parameters from the data collected with the LHCb detector, a maximum likelihood fit is performed. A detailed description of the used model, a probability density function, is given in chapter 4.

In this thesis an emphasis is given on the time resolution of the detector. A method was used to extract the resolution from the data. This method was validated

by applying this method to simulated events to estimate systematic uncertainties. This can be found in chapter 5.

To check the consistency of the fit, studies of the pull and error distributions have been done in chapter 6.

In chapter 7 a complete fit to the 2010 LHCb data has been performed. The found value of the CP violating parameter turned out to be in agreement with the current world average.

In the last chapter, two unbinned Goodness-of-Fit tests have been performed. The found statistical significances of  $p = 0.477$  and  $p = 0.812$  suggest that applied model does indeed correctly describe the data.

## B meson analysis

One of the most fundamental principles in physics is the connection between conservation laws and symmetries of nature. In particle physics certain discrete symmetries are found to be broken in physical interactions. The relevant discrete symmetries are:

- $C$  : charge conjugation changes the sign of all additive quantum numbers. With specific reference to the decay of a sub-atomic particle, charge conjugation consists of swapping every particle in the decay for its antiparticle.
- $P$  : the parity operation is the same as space inversion. It is the operation of reversing the direction of all three space coordinates.
- $T$  : the time reversal operator reverses the direction of motion by reflection in the time axis.

The combined CP-symmetry was proposed as the true symmetry between matter and antimatter after the discovery of parity violation in the weak interaction. In that scenario a process in which all particles are replaced by their antiparticles would be the same as the mirror image of the original process. However, this symmetry turned out to be violated as well and can be seen in the measurements of  $B^0 \rightarrow J/\psi K_S$ .

Although each of these three discrete symmetries is broken in weak interactions, the combined symmetry CPT is an exact symmetry in any local Lagrangian field theory.

## 2.1 The CKM matrix

The charged weak interaction is the only process in the standard model that does not conserve flavour. It can transform one type of quark into another one. Furthermore, there is mixing between the quark families. This is caused by the interaction eigenstates being different from the flavour eigenstates. The weak force couples to the pairs

$$\begin{pmatrix} u \\ d' \end{pmatrix}, \begin{pmatrix} c \\ s' \end{pmatrix} \quad \text{and} \quad \begin{pmatrix} t \\ b' \end{pmatrix}$$

with  $d'$ ,  $s'$  and  $b'$  linear combinations of mass eigenstates  $d$ ,  $s$  and  $b$ .

$$\begin{pmatrix} d' \\ s' \\ b' \end{pmatrix} = \begin{pmatrix} V_{ud} & V_{us} & V_{ub} \\ V_{cd} & V_{cs} & V_{cb} \\ V_{td} & V_{ts} & V_{tb} \end{pmatrix} \begin{pmatrix} d \\ s \\ b \end{pmatrix}$$

The matrix above that holds the coupling for the nine quark transitions is called the Cabibbo-Kobayashi-Maskawa matrix. From the unitarity of the CKM matrix, it follows that it contains four free parameters: three real and one complex phase.

A popular representation is the Wolfenstein parametrization, in which the magnitude of the couplings is readily seen. The parameter  $\lambda \approx 0.23$  and  $A, \rho, \eta$  are of order unity.

$$V_{\text{CKM}} = \begin{pmatrix} 1 - \frac{1}{2}\lambda^2 & \lambda & A\lambda^3(\rho - i\eta) \\ -\lambda & 1 - \frac{1}{2}\lambda^2 & A\lambda^2 \\ A\lambda^3(1 - \rho - i\eta) & -A\lambda^2 & 1 \end{pmatrix} + \mathcal{O}(\lambda^4)$$

Another instructive way is to make use of the angles:

$$\beta \equiv \arg \left[ -\frac{V_{td}V_{tb}^*}{V_{ud}V_{ub}^*} \right], \gamma \equiv \arg \left[ -\frac{V_{ud}V_{ub}^*}{V_{cd}V_{cb}^*} \right] \quad \text{and} \quad \beta_s \equiv \arg \left[ -\frac{V_{ts}V_{tb}^*}{V_{cs}V_{cb}^*} \right].$$

Any phase added to a specific quark cancels out, which make these definitions convention independent. Using the Wolfenstein phase convention the CKM can be written as

$$V_{\text{CKM}} = \begin{pmatrix} |V_{ud}| & |V_{us}| & |V_{ub}|e^{-i\gamma} \\ -|V_{cd}| & |V_{cs}| & |V_{cb}| \\ |V_{td}|e^{-i\beta} & -|V_{ts}|e^{i\beta_s} & |V_{tb}| \end{pmatrix} + \mathcal{O}(\lambda^5)$$

Later on in this chapter it is shown that the angle  $\beta$  is responsible for CP violation in  $B^0 \rightarrow J/\psi K_S$ .

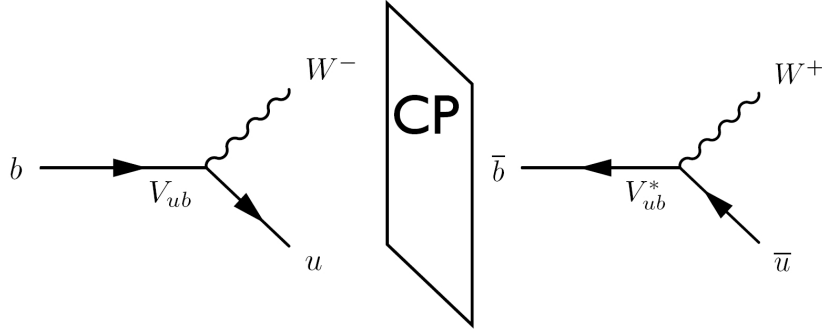


Figure 2.1: One of the flavour changing currents in the weak interaction, and its CP mirror image. The transition from a bottom quark to an up quark yields the factor  $V_{ub}$  in computation of the Feynman diagram. For the CP conjugate process, the factor is  $V_{ub}^*$ .

## 2.2 Mixing

The neutral B mesons are produced at the LHC in the flavour eigenstates

$$B^0 = (\bar{b}, d), \text{ and } \bar{B}^0 = (b, \bar{d})$$

The  $B^0$  can turn into its antiparticle  $\bar{B}^0$ , and vice versa,

$$B^0 \leftrightarrow \bar{B}^0$$

through a second-order weak interaction, as seen in figure 2.2. As a result, the

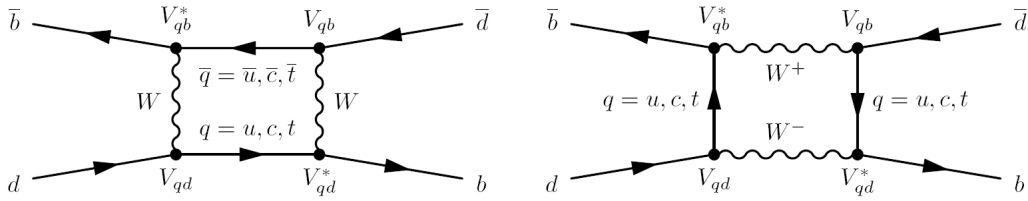


Figure 2.2: The dominant Feynman diagrams contributing to the mixing  $B^0 \leftrightarrow \bar{B}^0$ . The diagram with the top quark are the main contributors because of its high mass.

particles we observe in the laboratory are not  $B^0$  and  $\bar{B}^0$ , but rather some linear combination of the two,

$$\Psi(t) = a(t)|B^0\rangle + b(t)|\bar{B}^0\rangle.$$

The time evolution of this  $B^0$  system is described by an effective Hamiltonian,

$$i\frac{\partial}{\partial t}\Psi = \mathbf{H}\Psi.$$

The matrix  $\mathbf{H}$  can be written as the sum of two Hermitian matrices  $\mathbf{M}$  and  $\mathbf{\Gamma}$ ,

$$\mathbf{H} = \mathbf{M} - \frac{i}{2}\mathbf{\Gamma}.$$

CPT invariance implies

$$\langle B^0 | \mathbf{H} | B^0 \rangle = \langle \overline{B^0} | \mathbf{H} | \overline{B^0} \rangle,$$

which gives the extra constraints  $m_{11} = m_{22}$  and  $\Gamma_{11} = \Gamma_{22}$ .

$$\mathbf{M} = \begin{bmatrix} m & m_{12} \\ m_{12}^* & m \end{bmatrix} \quad \text{and} \quad \mathbf{\Gamma} = \begin{bmatrix} \Gamma & \Gamma_{12} \\ \Gamma_{12}^* & \Gamma \end{bmatrix}.$$

The off-diagonal terms  $m_{12}$  and  $\Gamma_{12}$  couple the two quantum states of our system. The term  $m_{12}$  describes  $B^0 \leftrightarrow \overline{B^0}$  via virtual states, from which the box diagram in figure 2.2 is the dominant contributor. The term  $\Gamma_{12}$  describes the transition via real states, e.g.  $B^0 \rightarrow \pi^0 \pi^0 \rightarrow \overline{B^0}$ , which turns out to be negligible.

Notice that  $\mathbf{H}$  itself is not Hermitian. The non Hermitian part describes the leaking out and into the subspace spanned by  $B^0$  and  $\overline{B^0}$ .

$$\frac{d}{dt}(|a|^2 + |b|^2) = \frac{\partial |\Psi|^2}{\partial t} = \frac{\partial \Psi^\dagger}{\partial t} \Psi + \Psi^\dagger \frac{\partial \Psi}{\partial t} = i\Psi^\dagger (\mathbf{H}^\dagger - \mathbf{H}) \Psi = -\Psi^\dagger \mathbf{\Gamma} \Psi$$

Calculating the eigenvalues of  $\mathbf{H}$  gives

$$\lambda_{H,L} = m - \frac{i}{2}\Gamma \pm \sqrt{(m_{12} - \frac{i}{2}\Gamma_{12})(m_{12}^* - \frac{i}{2}\Gamma_{12}^*)}$$

If we define the real part of the root term above  $\Delta m/2$  and the imaginary part  $\Delta\Gamma/4$ , the eigenvalues can be nicely written as

$$\lambda_{H,L} = \left( m \pm \frac{\Delta m}{2} \right) - \frac{i}{2} \left( \Gamma \pm \frac{\Delta\Gamma}{2} \right).$$

So  $\Delta m$  and  $\Delta\Gamma$  are the mass and lifetime difference between the two interaction eigenstates in the weak interaction. Writing the corresponding eigenstates as

$$|B_{L,H}\rangle = p|B^0\rangle \pm q|\overline{B^0}\rangle$$

we find  $p$  and  $q$  by solving

$$\mathbf{H} \begin{bmatrix} p \\ \pm q \end{bmatrix} = \lambda_{L,H} \begin{bmatrix} p \\ \pm q \end{bmatrix},$$

which gives

$$\frac{q}{p} = \sqrt{\frac{m_{12}^* - i\Gamma_{12}^*/2}{m_{12} - i\Gamma_{12}/2}}$$

In the case that  $|\frac{q}{p}| \neq 1$  we would have what is called CP violation in mixing, which has been observed in the neutral kaon system. It is a result of the mass eigenstates being different from the CP eigenstates. Doing some algebra, one can find that

$$\left|\frac{q}{p}\right| = \sqrt{\frac{1 - r \sin \phi + r^2}{1 + r \sin \phi + r^2}}, \quad r \equiv \left|\frac{\Gamma_{12}}{m_{12}}\right|, \quad \phi \equiv \arg(\Gamma_{12}) - \arg(m_{12})$$

From theoretical calculations it is known that  $r \ll 1$ , see [6]. The Taylor expansion is given by

$$\left|\frac{q}{p}\right| = 1 - \frac{1}{2}r \sin \phi + \mathcal{O}(r^2) \approx 1.$$

So CP violation in mixing is expected to be small in the  $B^0$  system. Furthermore the measured lifetime difference is very small [5],

$$\frac{\Delta\Gamma}{\Gamma} = -0.008 \pm 0.037,$$

and it will be set to zero to simplify the equations. Now that we found the eigenstates and eigenvectors, we know the time evolution of our system.

$$\begin{aligned} |B_H(t)\rangle &= |B_H\rangle e^{-i(m+\frac{1}{2}\Delta m)t} e^{-\frac{1}{2}\Gamma t} \\ |B_L(t)\rangle &= |B_L\rangle e^{-i(m-\frac{1}{2}\Delta m)t} e^{-\frac{1}{2}\Gamma t} \end{aligned}$$

## 2.3 Decay rate asymmetry

Because the neutral B mesons are produced in their flavour eigenstates, the time evolution has to be written in terms of them. For a particle created as a  $B^0$  at  $t = 0$ ,

$$\begin{aligned} |B^0(t)\rangle &= \frac{1}{2p}|B_L\rangle e^{-i\lambda_L t} + \frac{1}{2p}|B_H\rangle e^{-i\lambda_H t} \\ &= \frac{1}{2p} \left( p|B^0\rangle + q|\overline{B^0}\rangle \right) e^{-i\lambda_L t} + \frac{1}{2p} \left( p|B^0\rangle - q|\overline{B^0}\rangle \right) e^{-i\lambda_H t} \\ &= \frac{1}{2}|B^0\rangle \left( e^{-i\lambda_L t} + e^{-i\lambda_H t} \right) + \frac{q}{2p} |\overline{B^0}\rangle \left( e^{-i\lambda_L t} - e^{-i\lambda_H t} \right) \\ &= e^{-imt} e^{-\frac{\Gamma}{2}t} \left\{ |B^0\rangle \cos(\Delta m t/2) + i\frac{q}{p} |\overline{B^0}\rangle \sin(\Delta m t/2) \right\} \end{aligned}$$

The amplitude for a decay to a state  $f$ , at time  $t$  is given by

$$\begin{aligned}
A_{B^0(t) \rightarrow f}(t) &= \langle f|T|B^0(t)\rangle \\
&= e^{-imt} e^{-\frac{\Gamma}{2}t} \left\{ \langle f|T|B^0\rangle \cos(\Delta mt/2) + i\frac{q}{p} \langle f|T|\overline{B^0}\rangle \sin(\Delta mt/2) \right\} \\
&= e^{-imt} e^{-\frac{\Gamma}{2}t} \left\{ A_{B^0 \rightarrow f} \cos(\Delta mt/2) + i\frac{q}{p} A_{\overline{B^0} \rightarrow f} \sin(\Delta mt/2) \right\} \\
&= e^{-imt} e^{-\frac{\Gamma}{2}t} A_{B^0 \rightarrow f} \{ \cos(\Delta mt/2) + i\lambda \sin(\Delta mt/2) \}
\end{aligned}$$

In the last step we introduced the convenient parameter

$$\lambda \equiv \frac{q A_{\overline{B^0} \rightarrow f}}{p A_{B^0 \rightarrow f}}.$$

We find the time dependent decay rate by squaring the above expression

$$\begin{aligned}
\Gamma_{B^0(t) \rightarrow f} &= |A_{B^0(t) \rightarrow f}|^2 \\
&= e^{\Gamma t} |A_{B^0 \rightarrow f}|^2 |\cos(\Delta mt/2) + i\lambda \sin(\Delta mt/2)|^2 \\
&= e^{\Gamma t} |A_{B^0 \rightarrow f}|^2 \{ \cos^2(\Delta mt/2) + |\lambda|^2 \sin^2(\Delta mt/2) + i(\lambda - \lambda^*) \sin(\Delta mt) \} \\
&= \frac{e^{\Gamma t}}{2} |A_{B^0 \rightarrow f}|^2 \{ 1 + |\lambda|^2 + (1 - |\lambda|^2) \cos(\Delta mt) - 2\Im\lambda \sin(\Delta mt) \} \\
&= \frac{e^{\Gamma t}}{2} (1 + |\lambda|^2) |A_{B^0 \rightarrow f}|^2 \{ 1 + C \cos(\Delta mt) - S \sin(\Delta mt) \}
\end{aligned}$$

In the last step we introduced two other convenient parameters,

$$C \equiv \frac{1 - |\lambda|^2}{1 + |\lambda|^2} \quad \text{and} \quad S \equiv \frac{2\Im(\lambda)}{1 + |\lambda|^2}.$$

Doing the same calculation for the  $\overline{B^0}$  yields

$$\begin{aligned}
|\overline{B^0}(t)\rangle &= \frac{1}{2q} |B_L\rangle e^{-i\lambda_L t} - \frac{1}{2q} |B_H\rangle e^{-i\lambda_H t} \\
&= \frac{1}{2q} (p|B^0\rangle + q|\overline{B^0}\rangle) e^{-i\lambda_L t} - \frac{1}{2q} (p|B^0\rangle - q|\overline{B^0}\rangle) e^{-i\lambda_H t} \\
&= \frac{1}{2} |\overline{B^0}\rangle (e^{-i\lambda_L t} + e^{-i\lambda_H t}) + \frac{p}{2q} |B^0\rangle (e^{-i\lambda_L t} - e^{-i\lambda_H t}) \\
&= e^{-imt} e^{-\frac{\Gamma}{2}t} \left\{ |\overline{B^0}\rangle \cos(\Delta mt/2) + i\frac{p}{q} |B^0\rangle \sin(\Delta mt/2) \right\}.
\end{aligned}$$

The time dependent amplitude to the same state  $f$  as before is given by

$$\begin{aligned} A_{\overline{B^0}(t) \rightarrow f} &= \langle f | T | \overline{B^0}(t) \rangle \\ &= e^{-imt} e^{-\frac{\Gamma}{2}t} \left\{ \langle f | T | \overline{B^0} \rangle \cos(\Delta mt/2) + i \frac{p}{q} \langle f | T | B^0 \rangle \sin(\Delta mt/2) \right\} \\ &= e^{-imt} e^{-\frac{\Gamma}{2}t} \frac{p}{q} A_{B^0 \rightarrow f} \{ \lambda \cos(\Delta mt/2) + i \sin(\Delta mt/2) \}. \end{aligned}$$

By again squaring the amplitude we find the decay rate,

$$\begin{aligned} \Gamma_{\overline{B^0}(t) \rightarrow f} &= e^{\Gamma t} \left| \frac{p}{q} \right|^2 |A_{B^0 \rightarrow f}|^2 |\lambda \cos(\Delta mt/2) + i \sin(\Delta mt/2)|^2 \\ &= e^{\Gamma t} \left| \frac{p}{q} \right|^2 |A_{B^0 \rightarrow f}|^2 (|\lambda|^2 \cos^2(\Delta mt/2) + \sin^2(\Delta mt/2) + i(\lambda^* - \lambda) \sin(\Delta mt/2)) \\ &= \frac{e^{\Gamma t}}{2} \left| \frac{p}{q} \right|^2 |A_{B^0 \rightarrow f}|^2 (1 + |\lambda|^2 - (1 - |\lambda|^2) \cos \Delta mt + 2\Im \lambda \sin \Delta mt) \\ &= \frac{e^{\Gamma t}}{2} \left| \frac{p}{q} \right|^2 (1 + |\lambda|^2) |A_{B^0 \rightarrow f}|^2 (1 - C \cos \Delta mt + S \sin \Delta mt). \end{aligned}$$

If we take into account that  $|p| \approx |q|$ , the time dependent decay rate asymmetry is given by:

$$\begin{aligned} A_{CP}(t) &= \frac{\Gamma_{\overline{B^0}(t) \rightarrow f} - \Gamma_{B^0(t) \rightarrow f}}{\Gamma_{\overline{B^0}(t) \rightarrow f} + \Gamma_{B^0(t) \rightarrow f}} \\ &= S \sin(\Delta mt) - C \cos(\Delta mt). \end{aligned}$$

So the problem of finding CP violation in the decay modes of the  $B^0$  system is now reduced to determining the characteristic variable  $\lambda$ .

## 2.4 $B^0 \rightarrow J/\psi K_S$

A well known case is the asymmetry in the decay  $B^0 \rightarrow J/\psi K_S$  where the  $B^0$  can either directly decay to  $J/\psi K_S$  or oscillate to  $\bar{B}^0$  and then decay to  $J/\psi K_S$ . This interference between the mixed and unmixed decay amplitudes causes a CP violating asymmetry, the measurement of which was the first observation of CP violation in the B meson system.

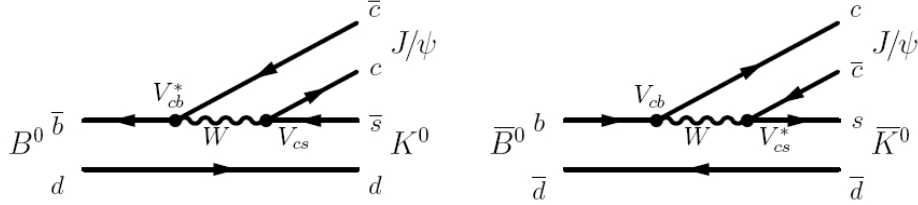


Figure 2.3: The dominant Feynman diagrams for  $B^0 \rightarrow J/\psi K^0$  and  $\bar{B}^0 \rightarrow J/\psi \bar{K}^0$ . The produced kaons oscillate between  $K^0 \leftrightarrow \bar{K}^0$ . The weak eigenstates are  $K_L$  and  $K_S$ , in analogy with  $B_H$  and  $B_L$ .

The  $B^0 \rightarrow J/\psi K_S$  mode is often named the gold-plated mode. It has a relatively large branching fraction and readily accessible final states with small backgrounds and is theoretically clean.

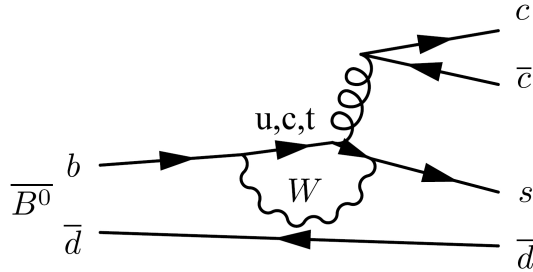


Figure 2.4: The dominant Penguin diagrams.

If we take the Penguin diagrams of figure 2.4 into consideration, the total amplitude is given by

$$A_{\bar{B}^0 \rightarrow J/\psi K^0} = V_{cb}V_{cs}^*T + V_{tb}V_{ts}^*P_s + V_{cb}V_{cs}^*P_c + V_{ub}V_{us}^*P_u,$$

where  $T$  and  $P_j$  stands for the tree and Penguin amplitudes. Using the unitarity

condition of the CKM matrix, this can be written as

$$A_{\overline{B}^0 \rightarrow J/\psi K_0} = \underbrace{V_{cb}V_{cs}^*(T + P_c - P_t)}_{\mathcal{O}(\lambda^2)} + \underbrace{V_{ub}V_{us}^*(P_u - P_t)}_{\mathcal{O}(\lambda^4)}$$

So the Penguin diagrams with a different weak phase than the tree diagrams are suppressed. This implies that there is no direct CP violation in decay, e.g.  $|A_{B^0 \rightarrow f}| = |A_{\overline{B}^0 \rightarrow f}|$ . It simplifies the decay rate asymmetry even further by making  $|\lambda| = 1$  and consequently  $C = 0$ .

$$A_{\text{CP}}(t) = S \sin(\Delta mt).$$

So this leaves us with determining the characteristic parameter  $\lambda$ . According to [7] it is given:

$$\lambda = \frac{q}{p} \frac{A_{\overline{B}^0 \rightarrow J/\psi K_S}}{A_{B^0 \rightarrow J/\psi K_S}} = - \left(\frac{q}{p}\right)_{B^0} \left(\frac{A_{\overline{B}^0 \rightarrow J/\psi \overline{K}^0}}{A_{B^0 \rightarrow J/\psi K^0}}\right) \left(\frac{p}{q}\right)_{K^0}$$

The factor  $-1$  accounts for the the final state  $J/\psi K_S$  being CP-odd and the additional  $\left(\frac{p}{q}\right)$  for the mixing of the kaons. From the box diagram of the  $B^0$  mixing we can see that  $m_{12} \propto V_{tb}^*V_{td}V_{tb}V_{td}$  and thus

$$\left(\frac{q}{p}\right)_{B^0} = \frac{V_{tb}^*V_{td}}{V_{tb}V_{td}^*}.$$

Doing the same thing for the  $K^0$  mixing gives

$$\left(\frac{p}{q}\right)_{K^0} = \frac{V_{cs}V_{cd}^*}{V_{cs}^*V_{cd}}.$$

By inspecting the Feynman diagrams of figure 2.3, we see that the ratio of the decay amplitudes is given by

$$\left(\frac{A_{\overline{B}^0 \rightarrow J/\psi \overline{K}^0}}{A_{B^0 \rightarrow J/\psi K^0}}\right) = \frac{V_{cb}V_{cs}^*}{V_{cb}^*V_{cs}}$$

Multiplying everything gives

$$\lambda = - \frac{\overline{V}_{tb}V_{td}V_{cb}\overline{V}_{cd}}{V_{tb}\overline{V}_{td}\overline{V}_{cb}V_{cd}} = -e^{-2i\beta}$$

with  $\beta$  the angle defined in section 2.1. This gives

$$S = \Im(\lambda) = -\Im\{\cos(2\beta) - i \sin(2\beta)\} = \sin(2\beta).$$

The standard model value of  $S = 0.830_{-0.033}^{+0.013}$ , according to a global analysis of measurements [15] which excludes its direct measurement.

In order to measure this asymmetry, two important ingredients are needed. Namely the resolution of the decay-time and the original flavour of the B meson. The uncertainties of these quantities will introduce a dilution on our signal, which will be discussed in section 3.1 and 5.2. It is given by

$$\begin{aligned} A_{\text{CP}}^{\text{observed}}(t) &= D_{\text{flavour}} \cdot D_{\text{resolution}} \cdot \sin(2\beta) \sin(\Delta mt) \\ &= (1 - 2\omega) \cdot e^{-\frac{1}{2}\Delta m^2 \sigma_t^2} \cdot \sin(2\beta) \sin(\Delta mt), \end{aligned}$$

with  $\omega$  the mistag prediction and  $\sigma_t$  the width of the time resolution.

So in order to measure  $\sin(2\beta)$  correctly, these two contributions need to be taken into consideration. In this thesis special attention is given to the dilution from the time resolution, although its effect is actually small in  $B^0 \rightarrow J/\psi K_S$ . In the  $B_s$ -system, where the mixing frequency  $\Delta m$  is much larger, it will play an important role.

In figure 2.5 this asymmetry in a 2010 Monte Carlo data-sample is shown.

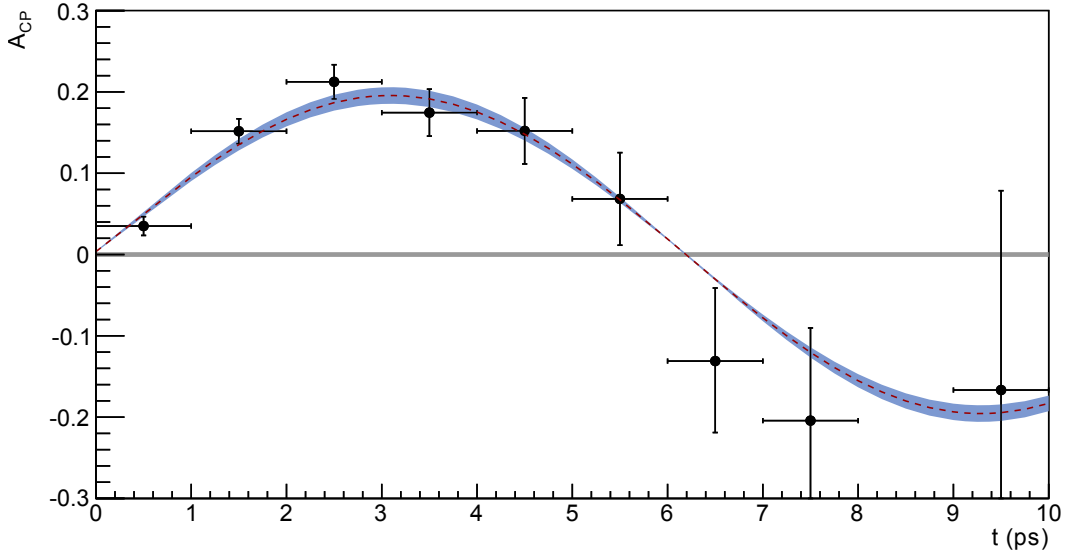


Figure 2.5: The time dependent CP asymmetry in  $B^0 \rightarrow J/\psi K_S$  from a MC10 sample with 72041 signal events. The dashed red curve is the p.d.f. overlaid to the data points. The blue band corresponds to the one standard deviation statistical error. The observed amplitude is much smaller than  $S$ . This is caused by the dilution from incorrect tagging and the finite time resolution.

## LHCb detector and data set

The  $B^0$ 's are produced at the interaction point of the proton collision, the primary vertex. A small fraction of these B mesons decay to  $J/\psi K^0$ . These daughter particles themselves also decay. The branching modes that are of interest are  $J/\psi \rightarrow \mu^+\mu^-$  and  $K_s \rightarrow \pi^+\pi^-$ . It are the tracks of these pions and muons that are actually measured in the LHCb detector and from them the  $B^0$ ,  $K_s$  and  $J/\psi$  are reconstructed, see figure 3.3.

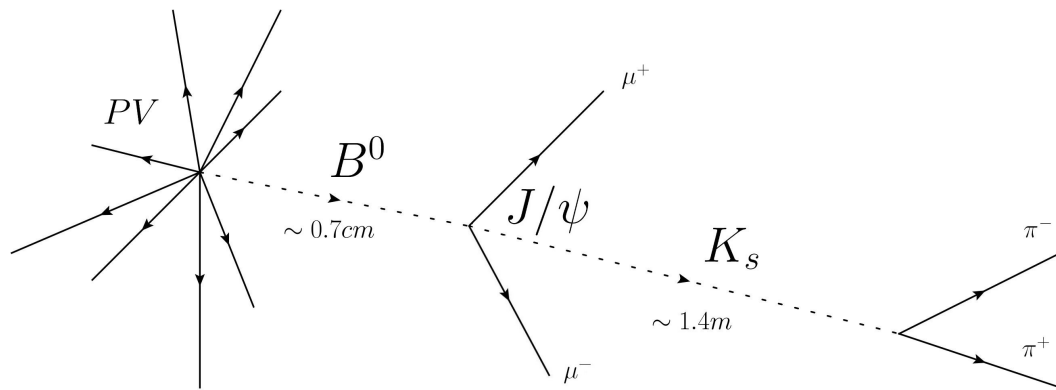


Figure 3.1: An artist impression of the topology of  $J/\psi K_s$ . The typical decay lengths are given by  $l = vt = v\gamma\tau = \frac{p}{m}\tau$ .

The LHCb detector, which is shown in figure 3.2, is a forward spectrometer. It has a polar angle coverage with respect to the beam line of approximately 15 to 300 mrad in the horizontal bending plane, and 15 to 250 mrad in the vertical non

bending plane. It has the following features:

### ***VELO***

The vertex locator is built around the proton interaction region. It is used to measure the particle trajectories close to the interaction point in order to precisely separate primary and secondary vertices.

### ***RICH-1***

The ring imaging Cherenkov detector is located directly after the vertex detector. It is used for particle identification of low-momentum tracks by measuring their velocity.

### ***Main Tracker***

The Main tracker consists of three parts.

- The Tracker Turicensis, a silicon strip detector located before the LHCb dipole magnet.
- The Outer Tracker. A straw-tube based detector located after the dipole magnet covering the outer part of the detector
- The Inner Tracker, silicon strip based detector located after the dipole magnet covering the inner part of the detector acceptance

### ***RICH-2***

Following the tracking system is RICH-2. It allows the identification of the particle type of high-momentum tracks.

### ***ECAL***

The electromagnetic and hadronic calorimeters provide measurement of the energy of electrons, photons, and hadrons. These measurements are used at trigger level to identify the particles with high transverse momentum.

### ***Muon System***

The muon system is used to identify and trigger on muons in the events.

Further details of the LHCb detector can be found in [2]. The used data sample from 2010 has an integrated luminosity of  $\mathcal{L} = 37\text{pb}^{-1}$ , an estimate of the yield  $N$

of  $B^0 \rightarrow J/\psi(\mu^+\mu^-)K_s(\pi^+\pi)$  is given by

$$\begin{aligned}
 N_{B^0 \rightarrow J/\psi(\mu^+\mu^-)K_s(\pi^+\pi)} &= \mathcal{L} \times 2 \times \sigma_{b\bar{b}} \times f_{b \rightarrow B^0} \\
 &\quad \times \text{BR}_{B^0 \rightarrow J/\psi K^0} \times \text{BR}_{K^0 \rightarrow K_S} \text{BR}_{J/\psi \rightarrow \mu^+\mu^-} \times \text{BR}_{K_s \rightarrow \pi^+\pi} \\
 &= 37 \text{ pb}^{-1} \cdot 2 \cdot 280 \mu\text{b} \cdot 0.4 \cdot 9\%_{00} \cdot \frac{1}{2} \cdot 6\% \cdot 70\% \\
 &= 0.16M.
 \end{aligned}$$

The overall efficiency of detecting these particles is around 1 %, so we expect the number of signal events to be of the order 1000.

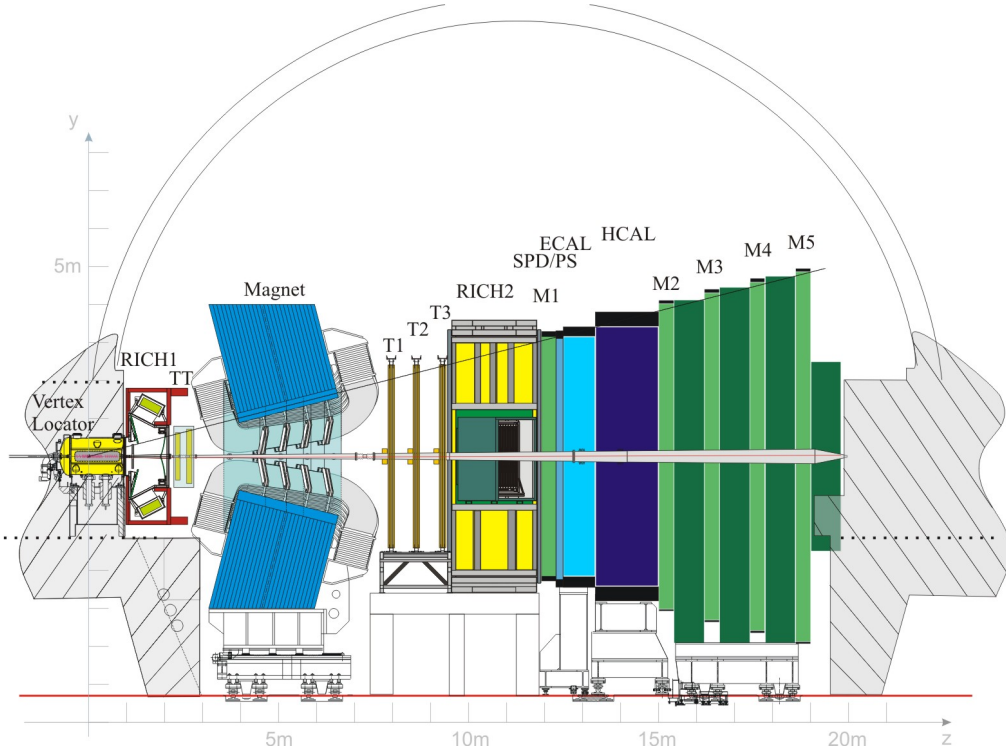


Figure 3.2: The LHCb detector and its components.

By cutting on measurement variables, the background is reduced to make the size of the data-sample manageable. These cuts are listed in table 3.1 and 3.2.

### 3.1 Flavour tagging

Flavour tagging determines whether the selected neutral B meson was born with a  $b$  or a  $\bar{b}$  quark. It is an essential part of the analysis. Without it one could

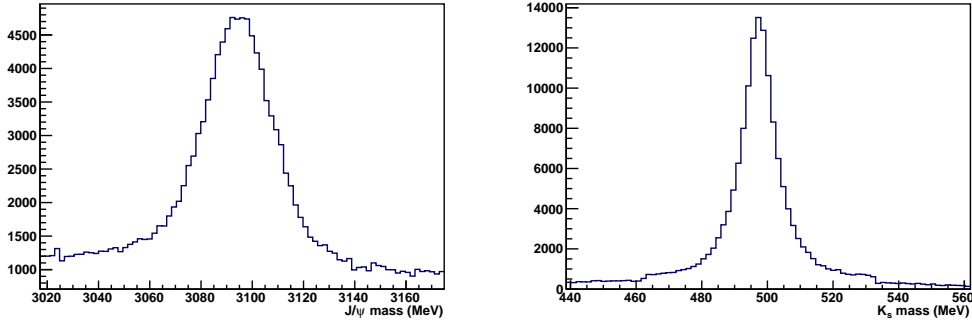


Figure 3.3: The invariant mass distribution of the reconstructed  $J/\psi$  and  $K_s$  candidate.

variable	cut value
$\chi^2$ of both $\mu$ tracks	$<5$
$\chi^2$ of the $J/\psi$ vertex	$<16$
window around $J/\psi$ mass	$<80$ MeV
DLL of both $\mu$	$>0$

Table 3.1: Stripping cuts to select the  $J/\psi$ . DLL is the difference in the log likelihoods of the particle being muon or a pion.

variable	cut value
$p_T$ of the $K_s$	$>1$ GeV
Decay length significance of the $K_s$	$> 5$
Momentum of both reconstructed $\pi$ 's	$>2$ GeV
IP significance of the downstream $\pi$ with respect to the PV	$>4$
IP significance of the long $\pi$ with respect to the PV	$>9$
$\chi^2$ of the $K_s$ vertex	$<20$
mass window around $K_s$ formed with downstream $\pi$	$<64$ MeV
mass window around $K_s$ formed with long $\pi$	$<35$ MeV

Table 3.2: Stripping cuts to select the  $K_s$ . A long  $\pi$ 's track starts at VELO. A downstream  $\pi$ 's track originates from the TT and thus less accurate.

not distinguish between their decay rates and thus not observe any CP asymmetry altogether.

The observed CP asymmetry is diluted by the fraction of events that is wrongly tagged  $\omega$ .

$$\begin{aligned} A_{\text{CP,obs}}(t) &= \frac{\Gamma_{\overline{B^0},\text{obs}} - \Gamma_{B^0,\text{obs}}}{\Gamma_{\overline{B^0},\text{obs}} + \Gamma_{B^0,\text{obs}}} \\ &= \frac{(1 - \omega)\Gamma_{\overline{B^0}} + \omega\Gamma_{B^0} - \omega\Gamma_{\overline{B^0}} - (1 - \omega)\Gamma_{B^0}}{(1 - \omega)\Gamma_{\overline{B^0}} + \omega\Gamma_{B^0} + \omega\Gamma_{\overline{B^0}} + (1 - \omega)\Gamma_{B^0}} \\ &= (1 - 2\omega)A_{\text{CP}} \end{aligned}$$

There are two strategies to determine the flavour of the B meson: opposite-side and same-side tagging.

In same-side tagging the flavour of the signal  $B$  meson is measured directly. When a  $B^0(\bar{b}d)$  is created in a  $pp$  collision an  $\bar{d}$  becomes available in the fragmentation process. In case the  $\bar{d}$  hadronises into a  $\pi^+(\bar{d}u)$ , the positive charge of the pion reveals the flavour of the  $B^0$  meson. This method suffer from the high abundance of pions in the detector, and is not used for this analysis.

In opposite-tagging the flavour of the other  $B$  meson is measured to determine the flavour of the signal  $B$  meson. This can be done by measuring the charge of the lepton in semileptonic decays, the charge of the kaon in  $b \rightarrow c \rightarrow s$  transitions or the charge of the inclusive secondary vertex reconstructed from  $b$  decay products. This method suffers from the problem that opposite meson also oscillates, and the wrong initial flavour can be determined.

To calibrate the mistag probabilities the  $B^+ \rightarrow J/\psi K^+$  control channel is used. Because the charge of B meson reveals its flavour, the measured and calculated mistag prediction can be compared to extract a correction function. More information on the flavour tagging can be found in [3].

## 3.2 Reconstruction software.

The analysis in this thesis is done with two types of data, simulated data based on Monte Carlo techniques and real data measured in the LHCb detector. Both these samples are treated equivalently. The same reconstruction program used to reconstruct particles in real data will be used for the MC data.

The LHCb software makes use of the C++ framework of Gaudi [9]. Within this framework there are several applications that take care of the different tasks such as event generation, detector simulation, and reconstruction.

### *Generation of particles.*

The collision of the protons is simulated by the the external program Pythia [10].

As output it gives the four-momentum of the created particles. For the handling of the physics of B decays another external program called EvtGen [11] is used. Both programs are steered by the Gaudi application known as Gauss.

***Interaction with the detector.***

The next part of the simulation deals with the generated particles passing through the LHCb detector. This step is done by Geant4 toolkit [12], from which an event display can be seen in figure 3.4. It takes care of the interaction with the matter of the detector, the bending of charged particles in the magnetic field, and the decay of the remaining particles.

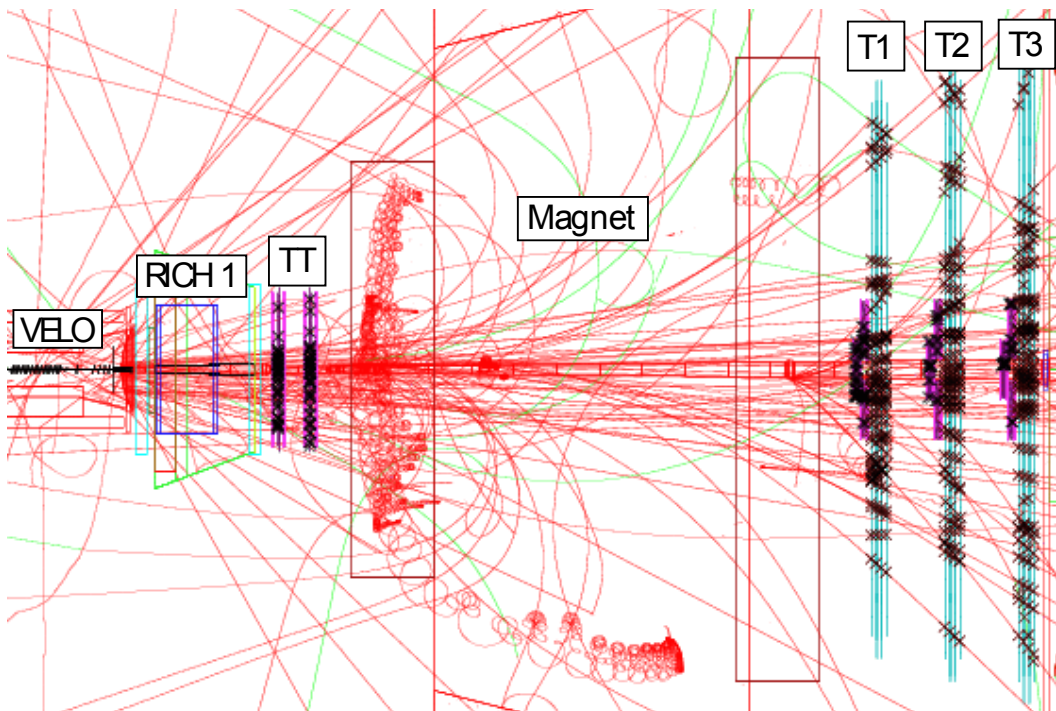


Figure 3.4: Geant event display showing the trajectories of the charged particles in the tracking system of LHCb.

***Digitization of the data.***

The next step is simulating the signal response of the sensors in the detector. This part of the simulation is done by the program Boole [13]. This response depends on physical processes like the production of electrons in a drift tube, or the specific behavior of the electronics. After this step there isn't a difference between the real raw data and the Monte Carlo simulated one.

***Track reconstruction.***

The last part is the track reconstruction. The hits from different sub-detectors are combined to find the trajectories of charged (meta-) stable particles namely pions, kaons, protons, muons, and electrons. Because there are a large amount of tracks in a typical event, statistical methods are used to obtain the best estimates for the track parameters. These are then used in the physics analysis to locate the primary and secondary vertices, and to calculate the invariant mass of particle combinations.



## Description of the used model

Statistical methods are needed in order to extract meaningful information from experimental data. A useful and often employed tool is a maximum likelihood fit. In this case a probability density function (pdf) is fitted to a distribution of observables which it is suppose to describe.

Given a sample space that holds the possible values that  $x$  can have, the probability to observe a value within the interval  $[a, b]$  is given by the pdf  $\mathcal{P}$  is

$$\Pr(a \leq x \leq b) = \int_a^b \mathcal{P}(x) dx.$$

The objective is to model the distribution of a set of observables  $\{\vec{x}_i\}$  in terms of a number of parameters  $\vec{\alpha}$ . These parameters can originate from the standard model, like  $\sin(2\beta)$ , or they can describe detector effects like the mass resolution  $\sigma_m$ .

### 4.1 Extended likelihood fit

A pdf has a probability density for each data-point  $\vec{x}_i$  and parameter values  $\vec{\alpha}$ ,

$$\mathcal{P}_i(x_i; \vec{\alpha}).$$

The likelihood function gives a measure of the likelihood of the data-points by taking the product of these values,

$$\mathcal{L} \equiv \prod_i^N \mathcal{P}_i(\vec{x}_i; \vec{\alpha}).$$

In a maximum likelihood fit, the values of the parameters  $\vec{\alpha}$  are chosen to obtain the highest value for  $\mathcal{L}$  and thus best describing the data-set given a certain  $\mathcal{P}$ .

Because it is generally easier in algorithms to add than to multiply,  $\ln \mathcal{L}$  is often used.

$$\ln \mathcal{L} = \ln \sum_i^N \mathcal{P}_i(\vec{x}_i; \vec{\alpha})$$

Often in data analysis one wants to determine the amount of signal and background in a data sample through a fit. The easiest approach is to define the composite pdf  $\mathcal{P}$  made from a signal component  $\mathcal{S}$  and a background component  $\mathcal{B}$ :

$$\mathcal{P}(x) = f\mathcal{S}(x) + (1 - f)\mathcal{B}(x)$$

Here  $f$  is the signal fraction, so  $\mathcal{P}$  is automatically normalized to one.

Often one is interested in the number of signal and background events, not the fraction. In that case it is easier to construct the pdf as

$$\mathcal{P}(x) = \mu_S \mathcal{S}(x) + \mu_B \mathcal{B}(x).$$

Now we use  $\mu_S$  and  $\mu_B$ , the expected number of signal and background events. By treating the number of observed events  $N$  as an observable, its error is automatically propagated. This is done by adding a Poisson term.

$$\begin{aligned} \mathcal{L} &= \frac{e^{-(\mu_S + \mu_B)} (\mu_S + \mu_B)^N}{N!} \prod_i^N \left[ \frac{\mu_S}{\mu_S + \mu_B} \mathcal{S}(x_i) + \frac{\mu_B}{\mu_S + \mu_B} \mathcal{B}(x_i) \right] \\ &= \frac{e^{-(\mu_S + \mu_B)}}{N!} \prod_i^N [\mu_S \mathcal{S}(x_i) + \mu_B \mathcal{B}(x_i)] \end{aligned}$$

Giving rise to the log likelihood function

$$\ln \mathcal{L} = -\mu_S - \mu_B - \ln N! + \sum_i^N [\mu_S \mathcal{S}(x_i) + \mu_B \mathcal{B}(x_i)]$$

The term  $\ln N!$  is irrelevant because it will not change by varying the values of the parameters.

## 4.2 Parametrization

Our  $B^0$  candidate is characterized by five observables,

$$\vec{x} = \{m, t, \sigma_t, d, \omega\},$$

namely a mass  $m$ , a lifetime  $t$ , a lifetime error  $\sigma_t$ , a discrete initial flavour  $d$  and a mistag prediction  $\omega$ .

The probability density function which has to predict the distribution of these observables, consists of four parts. It has a part for tagged and untagged events, which each a signal and background component.

### Mass

The measured mass for signal events is modeled as a Gaussian with mean  $m_m$  and width  $\sigma_m$ ,

$$\mathcal{M}_{\text{sig}}(m; m_m, \sigma_m) \propto e^{-\frac{(m-m_m)^2}{2\sigma_m^2}}.$$

The mass distribution for the background events is modeled as an exponential function with slope  $\alpha_m$ ,

$$\mathcal{M}_{\text{bkg}}(m; \alpha_m) \propto e^{\alpha_m m}.$$

### Lifetime

The lifetime of a  $B^0$  is reconstructed as

$$t = \frac{ml}{p}$$

with  $m$  the mass of the meson,  $p$  its momentum and  $l$  the distance between the primary and secondary vertex. The model that describes the distribution of these measured lifetimes  $t$  is made out of three components.

First the actual distribution of the lifetimes is needed. For this the decay rates from section 1 are taken, with the lifetime  $\tau = \frac{1}{\Gamma}$  and initial flavour  $d = 1$  for a  $B^0$  and  $d = -1$  for a  $\bar{B}^0$ . Furthermore the conditional observable  $\omega$  is introduced, which is the per event mistag probability.

$$\mathcal{T}_{\text{sig,tagged}}(t, d; \tau, \Delta m | \omega) \propto e^{-t/\tau} \{1 - d[1 - 2\omega]S \sin(\Delta mt) + d[1 - 2\omega]C \cos(\Delta mt)\}.$$

A large component of the data-set consist of untagged events that have no information whether our meson is more likely to be born as a  $B^0$  or as a  $\bar{B}^0$ . In this case  $d = 0$  and  $\omega = \frac{1}{2}$  and the signal component of the pdf reduces to

$$\mathcal{T}_{\text{sig,untagged}}(t; \tau) \propto e^{-t/\tau}.$$

Second there is a part that needs to account for the background in the measured signal. Most of the background contribution is coming from prompt events. These are random combinations of reconstructed particles originating from the primary vertex. Often a  $B^0$  candidate was actually a  $J/\psi$  and a  $K_S$  that were created at the proton interaction point who happen to have the invariant mass of a  $B^0$ . Because

there is no secondary vertex in this case  $t = l = 0$ . This contribution is modeled as delta function  $\delta(t)$ .

A substantial fraction of the background events come from long-lived decays. Since the tracks from  $J/\psi$  are recreated from muons, semi-leptonic  $B$  and  $D$  decays contribute to the 'long-lived' background, and so do incompletely reconstructed  $B^0 \rightarrow J/\psi$  decays.

$$\mathcal{T}_{\text{bkg}}(t; \tau_{\text{ml}}, \tau_{\text{ll}}, f_{\text{ml}}, f_{\text{ll}}) \propto (1 - f_{\text{ml}} - f_{\text{ll}})\delta(t) + f_{\text{ml}}e^{-t/\tau_{\text{ml}}} + f_{\text{ll}}e^{-t/\tau_{\text{ll}}}$$

Third, a resolution model is needed. It accounts for the difference of the actual lifetime (which can be signal or background) and the reconstructed value. It is being modeled as a triple Gaussian, which uses a predicted error on the lifetime  $\sigma_t$  as a conditional observable.

$$\mathcal{R}(t; t_{\text{m}}, s_1, s_2, f_1, f_2 | \sigma_t) = \sum_{i=1}^3 f_i \mathcal{G}(t, t_{\text{m}}, s_i \cdot \sigma_t),$$

with the fractions adding up to 1,

$$\sum_{i=1}^3 f_i = 1.$$

The resolution model is convolved with the true proper time distribution to obtain the observed proper time distribution, which will be discussed further next section.

### Total pdf

Assuming that the mass and lifetime pdfs factorize, the two total pdfs that will be simultaneously fitted can be written as

$$\begin{aligned} \mathcal{P}_{\text{tagged}}(\vec{x}; \vec{\alpha}) &= N_{\text{sig,t}} \mathcal{M}_{\text{sig}} \mathcal{T}_{\text{sig,tagged}} \otimes \mathcal{R} + N_{\text{bkg,t}} \mathcal{M}_{\text{bkg}} \mathcal{T}_{\text{bkg}} \otimes \mathcal{R} \\ \mathcal{P}_{\text{untagged}}(\vec{x}; \vec{\alpha}) &= N_{\text{sig,u}} \mathcal{M}_{\text{sig}} \mathcal{T}_{\text{sig,untagged}} \otimes \mathcal{R} + N_{\text{bkg,u}} \mathcal{M}_{\text{bkg}} \mathcal{T}_{\text{bkg}} \otimes \mathcal{R} \end{aligned}$$

with the the five observables

$$\vec{x} = \{m, t, d, \sigma_t, \omega\}$$

and the twenty one parameters

$$\vec{\alpha} = \{m_{\text{m}}, \sigma_{\text{m}}, \alpha_{\text{m}}, \tau, \Delta m, \omega, S, C, \tau_{\text{ml}}, \tau_{\text{ll}}, f_{\text{ml}}, t_{\text{m}}, \sigma_1, \sigma_2, \sigma_3, f_1, f_2, N_{\text{sig,t}}, N_{\text{bkg,t}}, N_{\text{sig,u}}, N_{\text{bkg,u}}\}.$$

Of these parameters, the actual physics parameters are abstracted are  $m_{\text{m}}, \tau, S$  and  $C$ . The mixing frequency  $\Delta m$  is put constant at  $0.507 \text{ps}^{-1}$  because it can be measured better in other decays.

# Calibration of the resolution model

The measured decay time  $t$  differs from the true time  $t'$ , due to the finite experimental resolution of the detector. The distribution of these errors is described by the so-called resolution model and denoted by

$$\mathcal{R}(t - t').$$

It is assumed that  $t'$  and  $t - t'$  are independent, e.g. knowing the lifetime does not change the probability for a certain error and vice versa. Their corresponding pdf's then factorize,

$$\mathcal{P}(t'|t - t') = \mathcal{T}(t') \cdot \mathcal{R}(t - t').$$

Because the experimenter has no direct access to  $t'$ , this variable has to be integrated out. Leaving the pdf  $\mathcal{P}$  that solely depends on the observed time  $t$ .

$$\begin{aligned} \mathcal{P}(t) &= \int_{-\infty}^{\infty} \mathcal{T}(t') \cdot \mathcal{R}(t - t') dt' \\ &= (\mathcal{T} \otimes \mathcal{R})(t). \end{aligned}$$

So the lifetime pdf turns out to be a convolution of the true lifetime distribution  $\mathcal{T}(t)$  and the resolution model  $\mathcal{R}(t)$ . The finite resolution leads to a dilution on the measured asymmetry. So consequently, accurate knowledge of  $\mathcal{R}(t)$  is required.

The effect of the resolution model on the signal part of the pdf can be seen in figure 5.2. As can be seen, the region where the resolution model can be extracted from data lies around zero lifetimes. This region however is totally dominated by

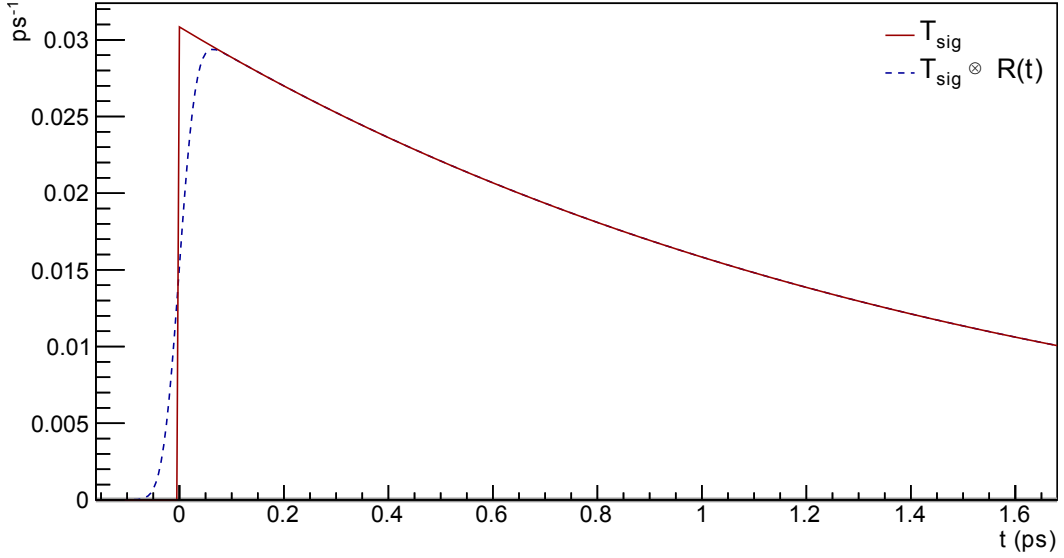


Figure 5.1: The effect of the resolution model on  $\mathcal{T}_{\text{sig}}(t)$

prompt events. So the model is effectively being calibrated on these prompt events. The shape of the prompt peak actually reveals the resolution function,

$$\mathcal{T}_{\text{P}}(t) \otimes \mathcal{R}(t) = \int_{-\infty}^{\infty} \delta(t') \cdot \mathcal{R}(t - t') dt' = \mathcal{R}(t).$$

A Monte Carlo study, reported in section 5.3, will shed light on the question if the resolution model is indeed comparable for the prompt and signal component.

## 5.1 Parametrization

A Gaussian measurement uncertainty on each lifetime  $t$  is modeled by

$$\mathcal{P}(t) = T(t) \otimes \mathcal{G}(t, \mu, \sigma).$$

The width  $\sigma$  stands for the experimental resolution and the mean  $\mu$  for the average bias.

The uncertainties in the vertex reconstruction and the momentum measurement give an error in the lifetime that differs from event to event. In first order it is given by

$$\sigma_t(t) \approx \sqrt{\left(\Delta l \frac{\partial t}{\partial l}\right)^2 + \left(\Delta p \frac{\partial t}{\partial p}\right)^2} = t \sqrt{\left(\frac{\Delta l}{l}\right)^2 + \left(\frac{\Delta p}{p}\right)^2}$$

Through assigning an experimental error  $\sigma_t$  to every measured value  $t$ , the statistical power of the model can be improved by

$$\mathcal{P}(t) = T(t) \otimes \mathcal{G}(t, \mu, s \cdot \sigma_t).$$

Events with the same  $t$  but a smaller  $\sigma_t$  will carry more information, because it will contribute more the total likelihood value.

The parameter  $s$  serves as a scale factor. If the error estimate  $\sigma_t$  is correct on average, a fit on data will return  $s = 1$ .

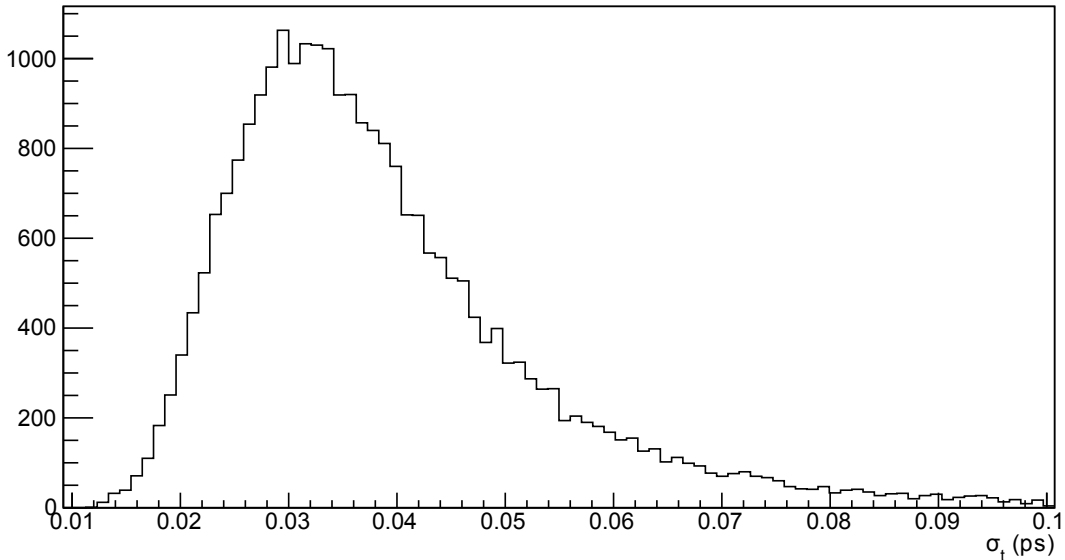


Figure 5.2: The distribution of the per event error  $\sigma_t$  in the 2010 LHCb data.

It turns out that to correctly describe the resolution model for  $B^0 \rightarrow J/\psi K_S$ , three Gaussians are needed

$$\mathcal{R}(t) = \sum_{i=1}^3 f_i \mathcal{G}(t, t_m, s_i \sigma_t),$$

The parameters of the resolution model are strongly correlated, e.g. a wider Gaussian can be accomplished a higher  $f_x$  or  $s_x$ . To compare the fitted values, the overall scale factor of the two smallest Gaussians are taken,

$$s_{\text{core}}(f_1, f_2, s_1, s_2) = \sqrt{\frac{f_1 s_1^2 + f_2 s_2^2}{f_1 + f_2}}.$$

Which can be written in easier notation as

$$s_{\text{core}}(\vec{x}) = \sqrt{\frac{x_1 x_3^2 + x_2 x_4^2}{x_1 + x_2}}.$$

The standard deviation of  $s_{\text{core}}$ , which will denote the error, is given by

$$s_{\text{err}} = \sqrt{\sum_{i,j=1}^4 \left[ \frac{\partial s_{\text{core}}}{\partial x_i} \frac{\partial s_{\text{core}}}{\partial x_j} \right] V_{ij}}.$$

with  $V_{ij}$  the covariance matrix of the parameters  $f_1$ ,  $f_2$ ,  $s_1$  and  $s_2$ .

## 5.2 Dilution

The convolution theorem states that Fourier Transform (FT) of the convolution of two functions equals the products of the FT of these functions. So

$$\text{FT}\{\mathcal{T} \otimes \mathcal{R}\}(\nu) = \sqrt{2\pi} \text{FT}\{\mathcal{T}\}(\nu) \times \text{FT}\{\mathcal{R}\}(\nu)$$

The Fourier transform of the resolution model is given by

$$\text{FT}\{\mathcal{R}\}(\nu) = \frac{1}{\sqrt{2\pi}} \sum_{i=1}^3 f_i e^{-\frac{1}{2}(s_i \sigma_t)^2 \nu^2}.$$

So the dilution to the amplitude of oscillation of frequency  $\Delta m$ , which is  $S$  in our analysis, is given by

$$D_{\text{res}} = \sum_{i=1}^3 f_i e^{-\frac{1}{2}(s_i \sigma_t)^2 \Delta m^2}.$$

## 5.3 Monte Carlo study.

To verify that the resolution function extracted from the prompt background is applicable to signal events, we compare the resolution on simulated data. The MC samples used is of type MC10.

For the signal component a  $B^0 \rightarrow J/\psi K_S$  sample is taken that underwent the same selection criteria as on the real data.

For the prompt component an inclusive  $J/\psi$  sample is used, with additional requirements on the reconstructed  $J/\psi$ 's and  $K_S$ 's. We want them to be correctly identified, they should not originate from a  $B^0$  and their vertici originate from the same point.

In figure 5.3 the samples are compared by their error  $t - t'$  and pull  $p = \frac{t-t'}{\sigma_t}$ . As can be seen the resolution models are in good correspondence with each other.

In figure 5.4 the predicted lifetime error  $\sigma_t$  dependency on the width of the time resolution is shown. The assumption of a linear relation is quite reasonable. The points that seem to deviate a bit have very low statistics and have a high lifetime error to begin with.

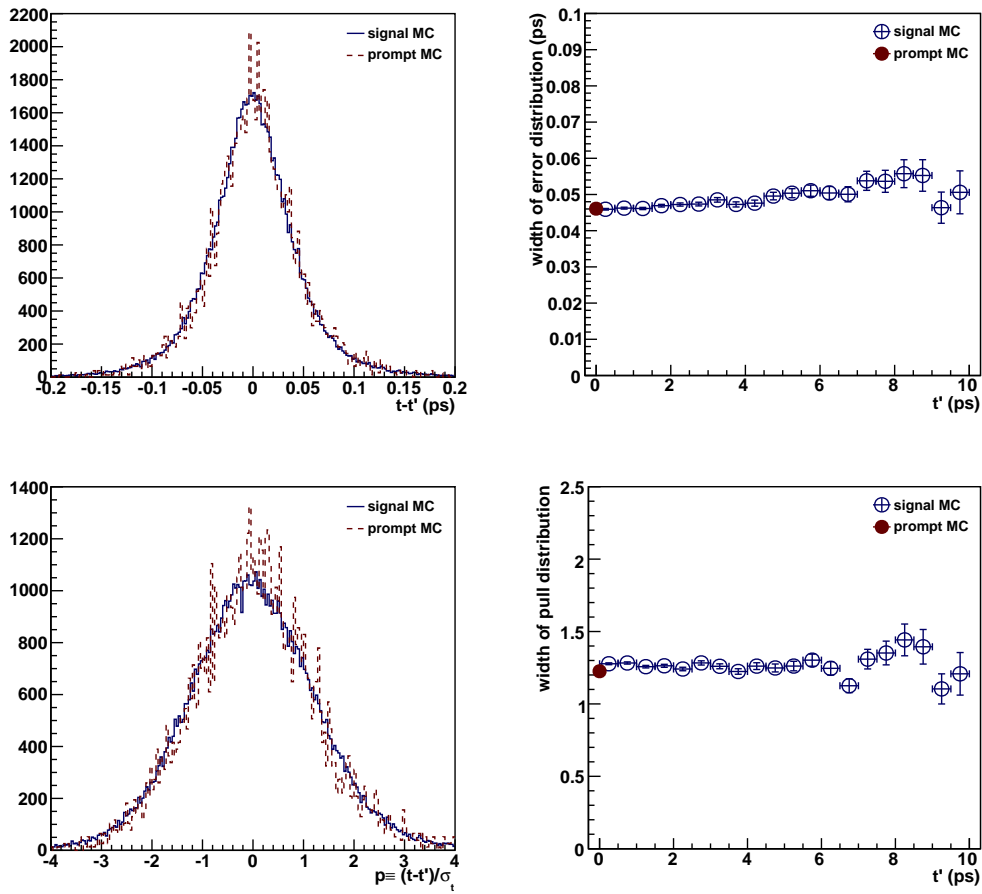


Figure 5.3: Comparison of the resolution of prompt MC (6074 events) and signal MC (79090 events). The distributions have been scaled by their integrals to compare their shapes. The two plots on the right show the width of the resolution model and the pull as a function of their true time  $t'$ .

Furthermore, other various variables have been investigated<sup>1</sup>, three of which are seen in figure 5.5. Although the distribution of these variables differ for the prompt and signal component, their dependence on the width of the resolution is the same.

<sup>1</sup>see appendix B for more

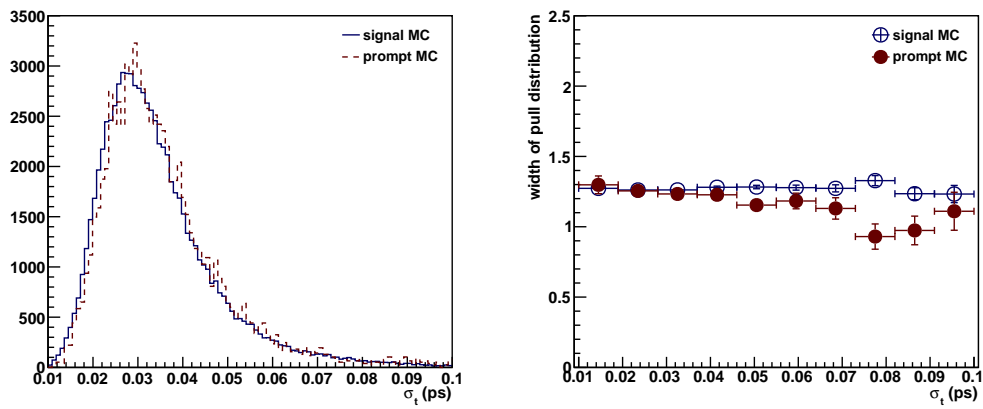


Figure 5.4: Resolution dependency of  $\sigma_t$  for prompt MC (6074 events) and signal MC (79090 events).

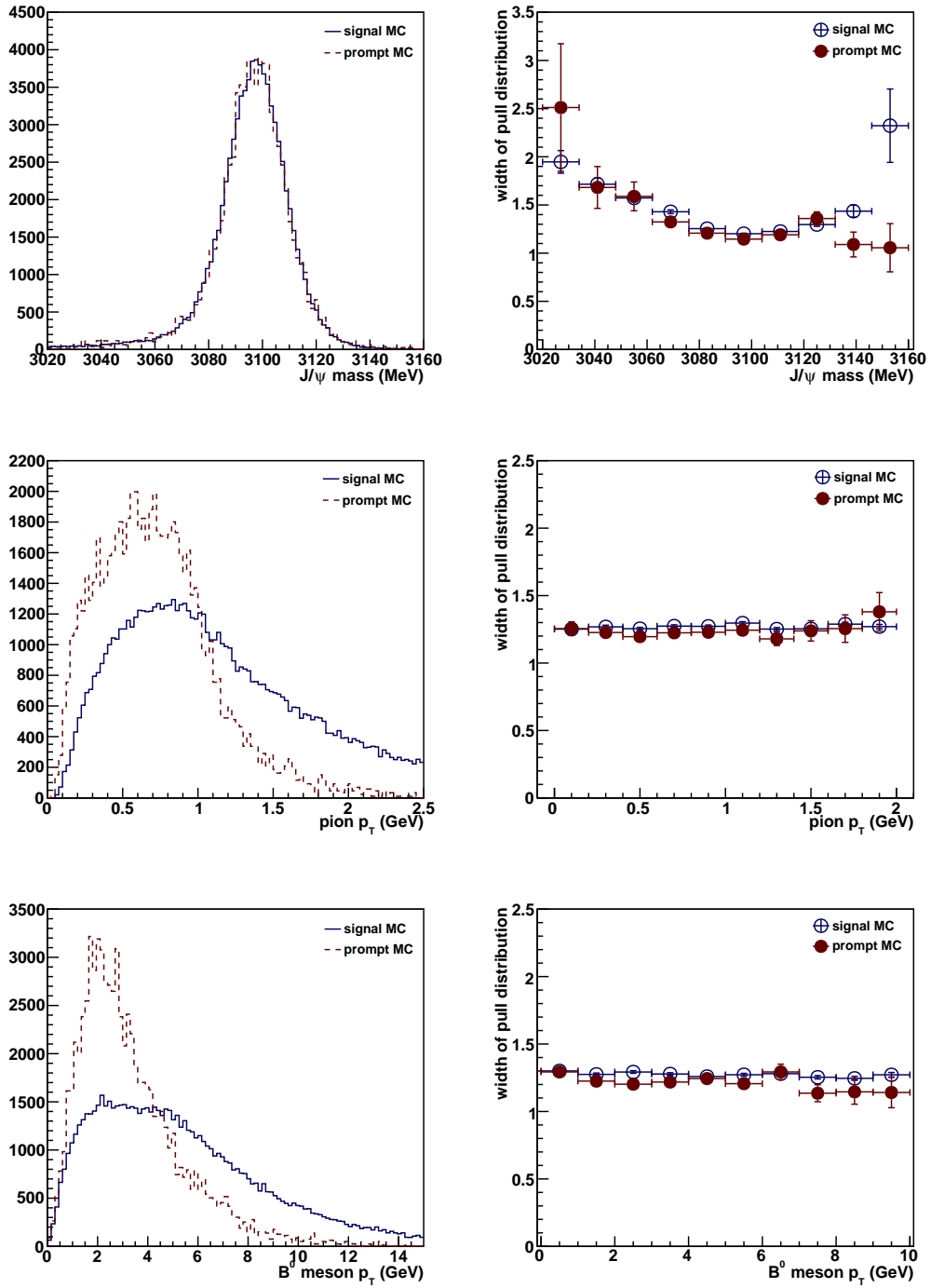


Figure 5.5: Comparison of the resolution dependencies of prompt MC (6074 events) and signal MC (79090 events).

To get a qualitative comparison, the root mean squared is calculated for the pull distribution of signal and prompt MC of figure 5.3 on the interval  $-4 < p < 4$ . This corresponds with 98.8 % of the signal events and 99.0% of the background events. The found values are

$$\begin{aligned}s_{\text{core,sig}} &= 1.2575 \pm 0.0040 \\ s_{\text{core,bkg}} &= 1.2178 \pm 0.014\end{aligned}$$

Using the width of the core, the dilution is roughly given by

$$D_{\text{res,MC}} \approx e^{-\frac{1}{2}(s_{\text{core}} \cdot \sigma_{t,\text{avg}})^2 \Delta m^2} = e^{-\frac{1}{2}(1.258 \cdot 0.035 \cdot 0.507)^2} = 1.00$$

So the time resolution is good enough that it doesn't play a role in determining the CP violation parameters in  $B^0 \rightarrow J/\psi K_S$ .

In other channels the resolution is of importance. In the analysis of  $B_s \rightarrow J/\psi \phi$  which has a similar resolution model, the dilution is estimated to be 0.68. This is caused by the higher mixing frequency  $17.8 \text{ ps}^{-1}$  of the  $B_s$  system. Here the time resolution limits the accuracy at which the oscillation can be measured.

## Validation of the fit.

As a test of the consistency of the fit, studies of the pull and error distributions have been done. To do this toy samples have been generated with the the central values of the parameters extracted from the fit to the full data sample, which are reported in chapter 7.

The pull of  $S$  and  $C$  are compatible with a standard normal distribution<sup>1</sup>, as can be seen figure 6.1 and 6.3.

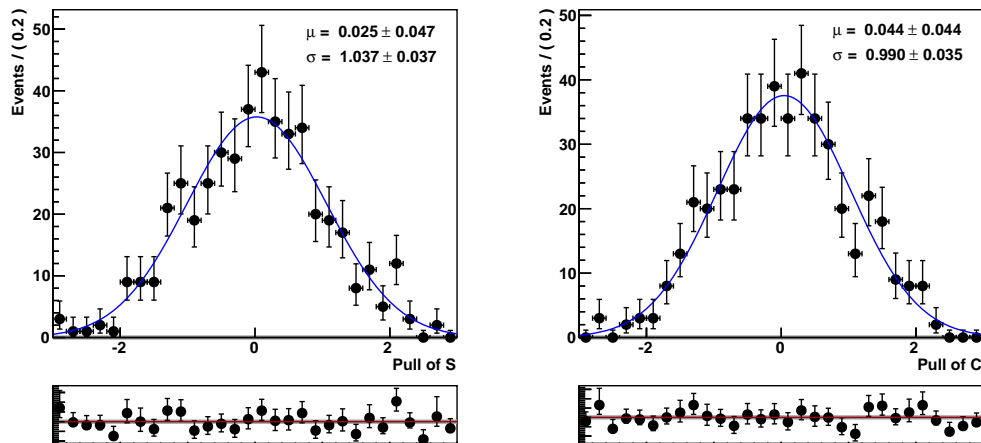


Figure 6.1: The pull distribution of  $S$  and  $C$  are compatible with a standard normal distribution.

<sup>1</sup>The other parameters can be found in appendix B

The distribution of the errors can be seen in figure 6.1 and 6.3. The found values for the errors on  $S$  and  $C$  in the data (reported in chapter 7) are a bit on the low end of the spectrum. They are within one standard deviation, so it is reasonable to regard this a lucky statistical fluctuation.

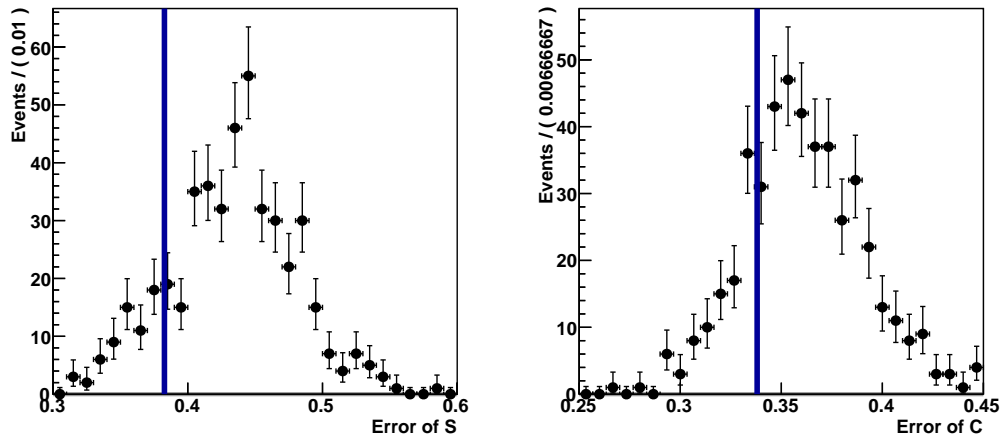


Figure 6.2: The error distribution of  $S$  and  $C$ . The vertical line indicates value of the fit to real data, reported in section 7.

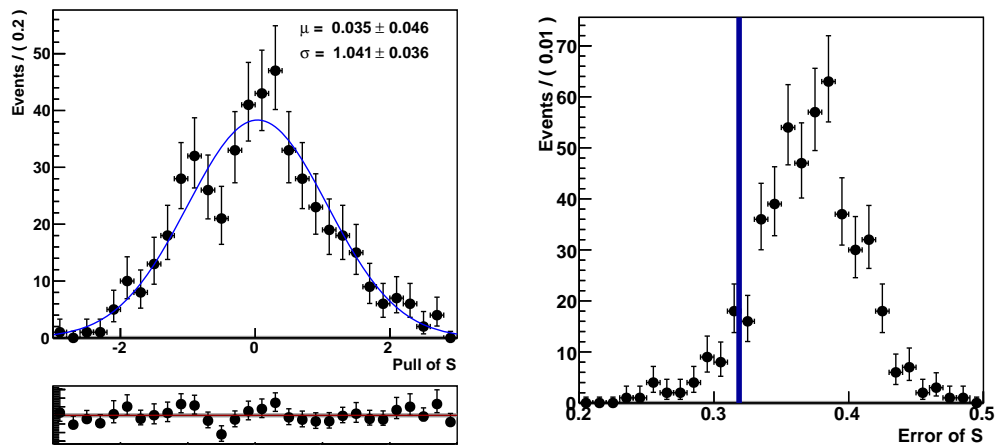


Figure 6.3: The pull and error distribution of  $S$ , but this time with  $C$  fixed.

Note that the spread in the error is large. This is due the small number of

tagged events which are consequently subjected to large fluctuations.



## Fit to 2010 data

The complete fit, described in section 2, was run on the 2010 data. It was done both done with and without  $C$  fixed to zero. The

The fit results for the physics parameters are summarized in table 7.1.

Figure 7.1, 7.2 and 7.3 show the data and pdf projections on the reconstructed mass and proper time. By using a logarithmic scale, the distribution over the entire lifetime range is revealed. The prompt component of the data is displayed by using a linear scale over the range  $t \in [-0.2; 0.2]$ .

As can be seen, the data seems to be well described by our model. In section 8, we will quantify this observation with the use of Goodness-of-Fit tests.

Parameter	Unit	Floating $C$	Fixed $C$
$C$		$0.279^{+0.340}_{-0.337}$	0
$S$		$0.720^{+0.394}_{-0.368}$	$0.881^{+0.334}_{-0.301}$
$m_m$	MeV	$5278.11 \pm 0.34$	$5278.11 \pm 0.34$
$m_s$	MeV	$8.77 \pm 0.28$	$8.77 \pm 0.28$
$\tau$	ps	$1.516 \pm 0.056$	$1.517 \pm 0.056$
$m_{s1}$	1/MeV	$-0.0006256 \pm 0.000089$	$-0.0006256 \pm 0.000089$
$\tau_{l1}$	ps	$1.01 \pm 0.20$	$1.01 \pm 0.19$
$\tau_{m1}$	ps	$0.220 \pm 0.034$	$0.220 \pm 0.032$
$f_{l1}$		$0.0071 \pm 0.0027$	$0.0071 \pm 0.0026$
$f_{m1}$		$0.0369 \pm 0.0031$	$0.0369 \pm 0.0031$
$t_m$	ps	$-0.000981 \pm 0.00028$	$-0.000981 \pm 0.00028$
$s_1$		$0.732 \pm 0.030$	$0.732 \pm 0.029$
$s_2$		$1.621 \pm 0.046$	$1.621 \pm 0.045$
$s_3$		$6.38 \pm 0.56$	$6.38 \pm 0.55$
$f_2$		$0.532 \pm 0.034$	$0.532 \pm 0.032$
$f_3$		$0.0162 \pm 0.0032$	$0.0162 \pm 0.0031$
$N_{\text{bkg,t}}$		$2907 \pm 54$	$2907 \pm 54$
$N_{\text{bkg,u}}$		$21610 \pm 148$	$21611 \pm 148$
$N_{\text{sig,t}}$		$198 \pm 16$	$198 \pm 16$
$N_{\text{sig,u}}$		$761 \pm 32$	$761 \pm 32$

Table 7.1: Fit results

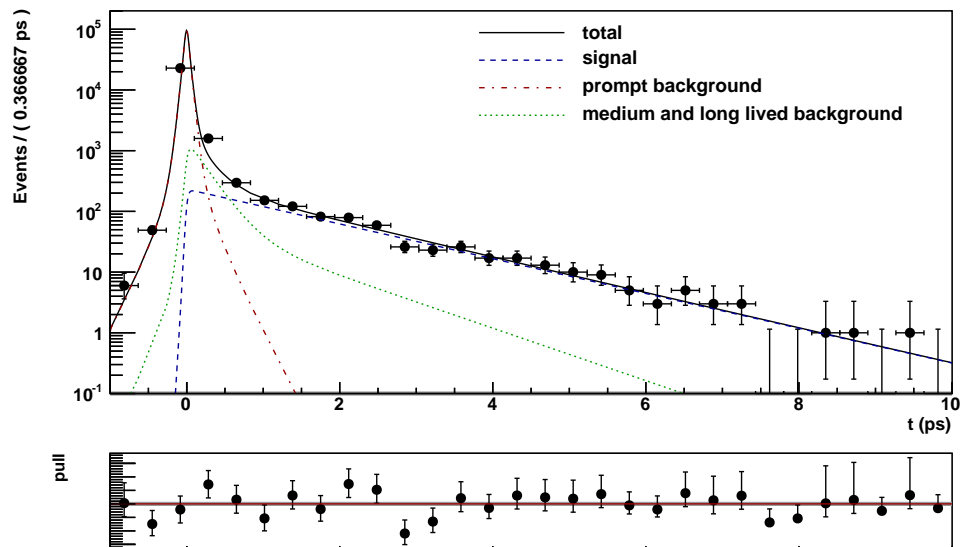


Figure 7.1: The distribution of the measured  $B$  lifetimes in 2010 data. The various components of  $\mathcal{P}$  are projected over it

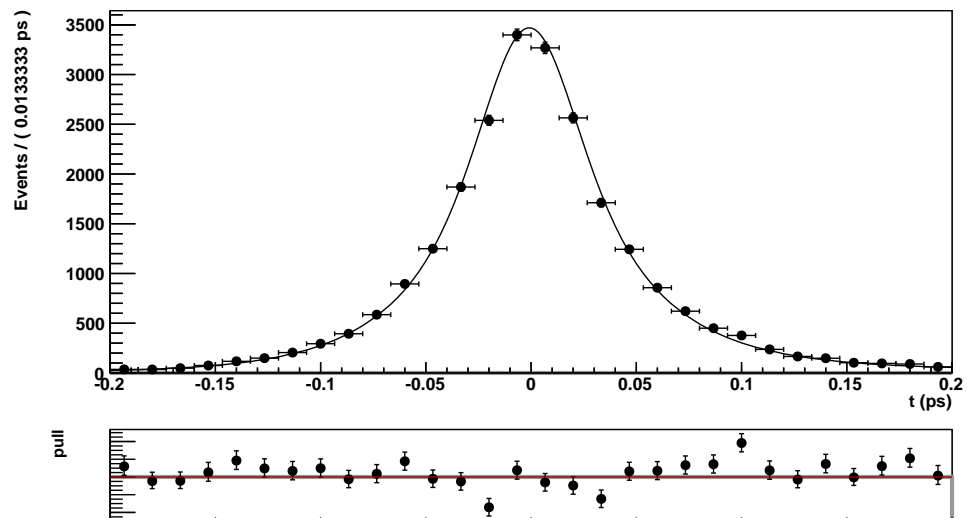
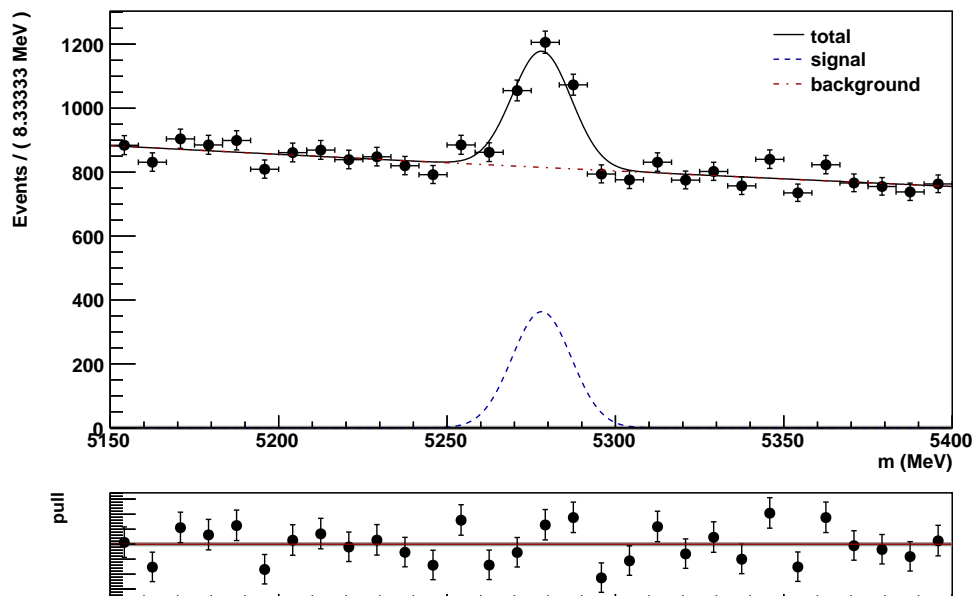


Figure 7.2: The distribution of the prompt component in the  $B$  lifetimes.

Figure 7.3: The distribution of measured  $B$  masses.

## 7.1 Systematic errors

In this section we investigate what qualitative effect the resolution model has on the other fitted parameters. A second fit is done with the width of the resolution model for the signal component scaled by the ratio found in the MC study  $\alpha = 1.3512/1.275$ .

$$\mathcal{R}_{\text{sig}}(t) = \sum_{i=1}^3 f_i \mathcal{G}(t, t_m, \alpha \cdot \sigma_i dt)$$

As can be seen in table 7.2 this has no measurable effect. So therefore we can safely conclude that using the same resolution model for signal and background events is justified.

Parameter	Unit	Value
$S$		$-0.880 \pm 0.32$
$m_m$	MeV	$5278.11 \pm 0.34$
$m_s$	MeV	$8.77 \pm 0.29$
$\tau$	ps	$762 \pm 32$
$m_{s1}$	1/MeV	$-0.0006256 \pm 0.000089$
$\tau_{11}$	ps	$1.01 \pm 0.20$
$\tau_{m1}$	ps	$0.220 \pm 0.035$
$f_{11}$		$0.0071 \pm 0.0028$
$f_{m1}$		$0.0368 \pm 0.0031$
$t_m$	ps	$-0.000994 \pm 0.00029$
$s_1$		$0.731 \pm 0.026$
$s_2$		$1.619 \pm 0.037$
$s_3$		$6.36 \pm 0.52$
$f_2$		$0.533 \pm 0.028$
$f_3$		$0.0163 \pm 0.0029$
$N_{\text{bkg,t}}$		$2908 \pm 54$
$N_{\text{bkg,u}}$		$21610 \pm 148$
$N_{\text{sig,t}}$		$197 \pm 15$
$N_{\text{sig,u}}$		$762 \pm 32$

Table 7.2: Fit result of using the scaled  $\mathcal{R}_{\text{sig}}$ .

The third Gaussian of the resolution is there to justify the more unlikely events in the data. As an alternative, a so-called 'garbage collector' could be used. This is a small constant component in the lifetime distribution, as can be seen in figure 7.4.

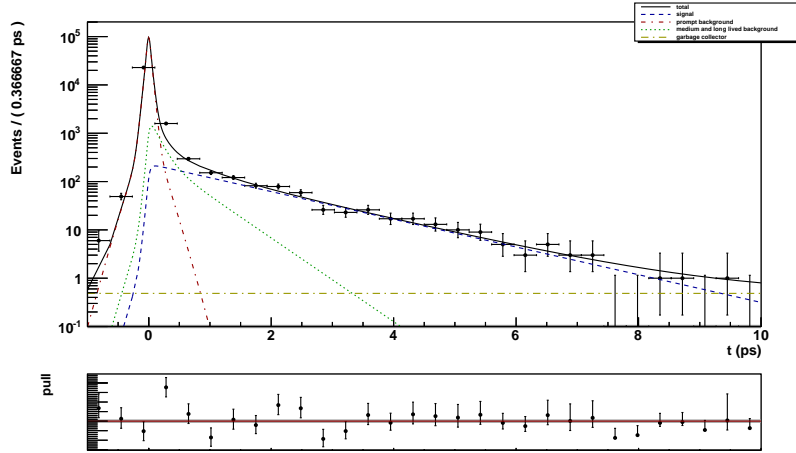


Figure 7.4: Using a garbage collector in the lifetime pdf

The fit results of table 7.3 shows that this renders the third Gaussian obsolete, without changing the values of the other fitted parameters. The physical argument for such a function can be debated however.

Parameter	Unit	Value
$t_m$	ps	$-0.001122 \pm 0.00037$
$s_1$		$0.705 \pm 0.052$
$s_2$		$1.55 \pm 0.12$
$s_3$		$5 \pm 10$
$f_2$		$0.561 \pm 0.057$
$f_3$		$0.024 \pm 0.019$

Table 7.3: Fit results using a a garbage collector. The other fitted parameters did not change from table 7.1.

Other systematic uncertainties have studied in detail in [4]. The total systematic uncertainty on  $S$  is calculated to be 0.054. The correct initial flavour identification of the neutral B meson gives the highest systematic error. It leads to additional uncertainty on  $S$  of about 10 %. This uncertainty is dominated by the statistics in the flavour tagging calibration channel.

## Goodness-of-Fit

In this analysis we want to determine the level of agreement between the fitted pdf  $\mathcal{P}$  and the 2010 LHCb data it should describe.

The plots of the previous section gave us an visual indication. In this section we investigate two quantitative Goodness-of-Fit methods.

In both cases a test statistic  $T$  quantifies the agreement, where a larger value means a bigger disagreement. By generating data-sets with  $\mathcal{P}$  and running the goodness-of-fit on them, the distribution of the test statistic  $g(T)$  is determined.

From this distribution we find the probability  $p$  of obtaining a test statistic at least as extreme as the one that was actually observed,

$$p = \int_T^{\infty} g(T') dT',$$

assuming that  $\mathcal{P}$  describes the data. We reject  $\mathcal{P}$  when  $p$  is less than a certain significance level  $\alpha$ , which in literature is often chosen to be 0.05 or 0.01.

In both methods we need to define distance in a multivariate space. The option used is normalized Euclidean distance,

$$|\vec{x}_i - \vec{x}_j|^2 = \sum_{v=1}^D \left( \frac{x_i^v - x_j^v}{w_v} \right)^2,$$

with  $w_v$  the appropriate normalization for the given dimension. The mass and time are the only two continuous unconditional observables, so we are dealing with the two dimensional case. The normalizations are chosen to be of the order of their respective resolution widths,  $w_m = 10$  MeV and  $w_t = 0.05$  ps.

## 8.1 Distance to Nearest Neighbor

In a region where  $\mathcal{P}$  is larger, the events will be closer together on average. This can be used to test the goodness of our fit. The uniformity  $U_i$  for the  $i^{\text{th}}$  event in the data consisting of  $n$  events is defined as

$$\ln U_i = -n \int_{A_i} \mathcal{P}(\vec{x}) d\vec{x}.$$

The area of integration  $A_i$  is the circle given by

$$A_i = |\vec{x} - \vec{x}_i| < r_i,$$

with  $r_i$  the distance from the  $i^{\text{th}}$  event to its nearest neighbor.

If we assume that the circle is sufficiently small so that  $\mathcal{P}$  is approximately constant in it, we can avoid having to do the integral. Then

$$\ln U_i \approx -n\pi r_i^2 \cdot \mathcal{P}(\vec{x}_i),$$

In case  $\mathcal{P}$  is the parent of the data, the distribution of  $U$  is approximately uniform.<sup>1</sup> In figure 8.1 the uniformity distribution is shown.

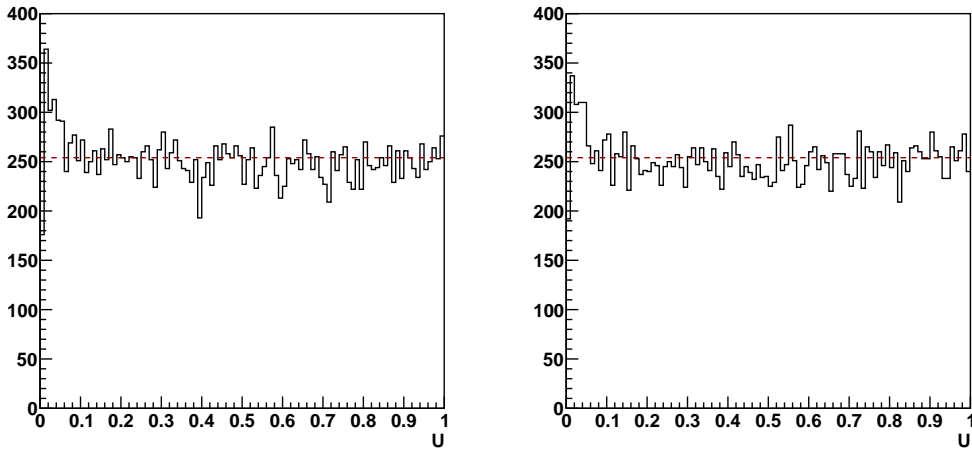


Figure 8.1: The uniformity distribution from the 2010 LHCb data is shown in the plot on the left. On the right the distribution from a generated toy.

---

<sup>1</sup>See Appendix A

The test statistic  $T$  is chosen to be

$$T = \sum_i^n (U'_i - i/n)^2$$

where  $\{U'_i\}$  is the ordered set of uniformity.

The distance to nearest neighbor method applied to the data gave a  $p = 0.812$ , which suggests that  $\mathcal{P}$  is correctly parametrized.

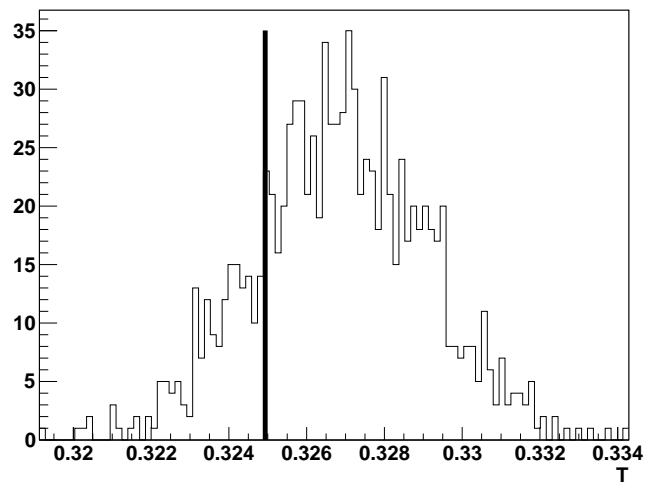


Figure 8.2: With the distance to nearest neighbor method the test statistic  $T = 0.325$ . The number of toys that had worse agreement with this test are 812 out of a 1000, giving  $p = 0.812$ .

## 8.2 Local-Density Method

The local density of data-points in the data can be compared to the number predicted by  $\mathcal{P}$  as a goodness of fit test.

The expected number of data-points  $e_i$  in a circle of radius  $R$  centered at a data-point with coordinates  $(r_i, \phi_i)$  is given by

$$\begin{aligned} e_i &= n \int_0^{2\pi} \int_0^R f(r, \phi) r \, dr d\phi \\ &\approx \pi N R^2 f(r_i, \phi_i), \end{aligned}$$

if we again assume that the region is small enough to consider  $\mathcal{P}$  constant.

In the scatter plot of figure 8.3 we see that the discrepancy between the observed and expected number of events becomes bigger for higher values of  $e$ . This is to be expected because in regions where  $\mathcal{P}$  is higher it also fluctuates more. The assumption that  $\mathcal{P}$  is constant is thus less accurate.

One way to damp this effect is to take  $e$  constant and vary the size of the circle accordingly. Then in a region where the  $\mathcal{P}$  changes more rapidly a smaller area is taken. From the plot  $e = 40$  seems to be reasonable, the smaller it is chosen the bigger the bias on the observed events.

The test statistic is chosen to be the average normalized error,

$$T = \frac{1}{n} \sum_{i=1}^n \frac{|o_i - e|}{e}.$$

An unlikely event can blow up the area and make a very big contribution to the test statistic. By taking an upper limit on  $R_i$ , we choose to be more sensitive for overall discrepancy than local ones, see figure 8.4.

The local density method applied to the data gave a  $p = 0.477$ , which again suggests that  $\mathcal{P}$  is correctly parametrized.

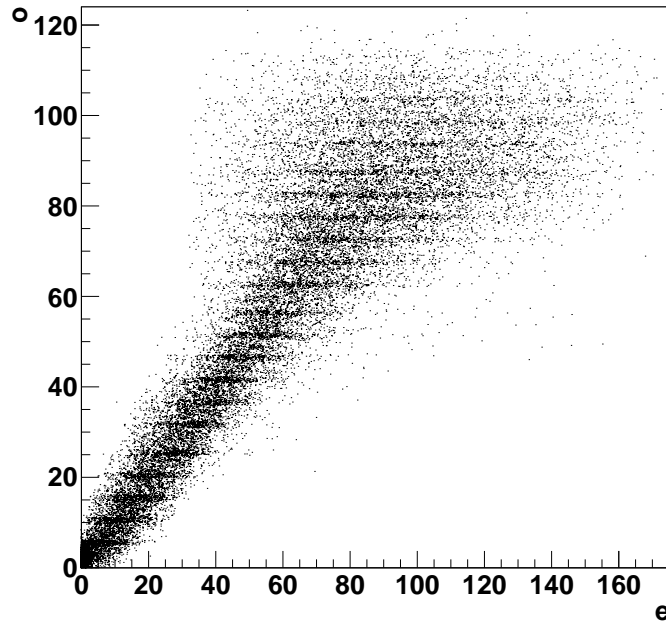


Figure 8.3: A scatter plot of the observed versus the expected events. The radius of the circle for the local density method was taken to be  $R = 0.003\sqrt{t_{\max}m_{\max}}$

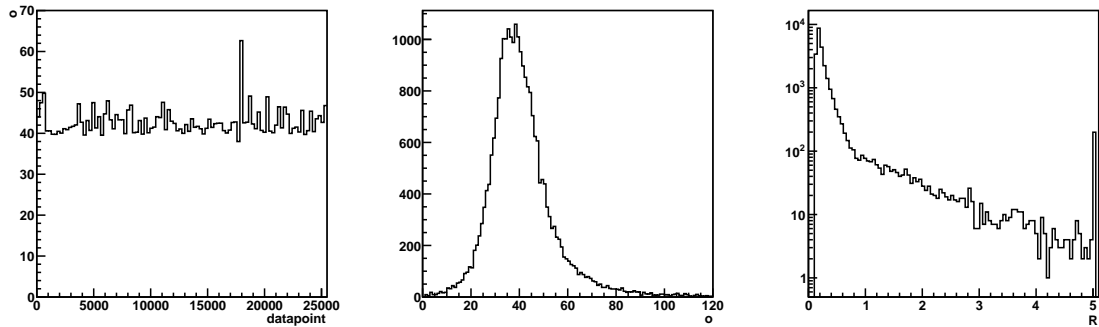


Figure 8.4: Local density method with  $e = 40$ . In the left graph we see the observed versus the data-points. The middle graph is the distribution of the observed events. The graph on the right is the distribution of the radius of the circle, which had a set upper limit of  $R = 5$ .

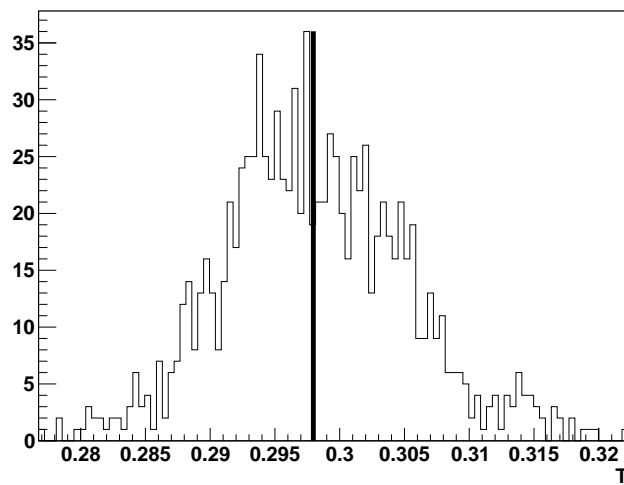


Figure 8.5: With the local density method the test statistic  $T = 0.298$ . The number of generated toys that had worse agreement with this test are 477 out of a 1000, giving  $p = 0.477$ .

## Conclusion & Outlook

The fit on the 2010 LHCb data found an time dependent asymmetry amplitude of

$$S = 0.881_{-0.301}^{+0.334}.$$

This is compatible with the current world average of  $S = 0.673 \pm 0.023$  [5], but not yet competitive. Another fit has been performed with floating  $C$ . The fitted values of the  $CP$  parameters then turn out to be

$$\begin{aligned} S &= 0.720_{-0.368}^{+0.394} \\ C &= 0.279_{-0.337}^{+0.340}. \end{aligned}$$

The value of  $C$  is compatible with the Standard Model prediction, which is zero. Furthermore it agrees with the latest results of the BaBar and Belle experiments, see [8] and [7]. It is pleasing to see, not to mention crucial for the collaboration, that analysis is in a mature state at LHCb and that it is in agreement with other experiments.

An important aim of the research presented in this thesis was to show that the resolution function obtained from the background events is representative for signal events. The Monte Carlo study did reveal this. What also was shown, is that resolution function is not really of importance in this particular analysis. However in similar decay modes of the  $B_s$ , a good time resolution is needed, because of the higher mixing frequency. Here it needs to be justified that the resolution model is calibrated on prompt events, which we now can.

Finally, the Goodness-of-Fits tested indicated that the used model indeed describes the data. It would be worthwhile to perform studies similar to this on other analysis. The distance to nearest neighbor method requires very little processing time and gives a quick visual diagnostic tool. The local density method is excellent

in giving an quantifiable level of agreement between between the model and the data.

It is expected that at the end of 2012 the integrated luminosity will be around  $2 \text{ fbarn}^{-1}$ . This entails roughly 54 times more data in comparison to this analysis, and it reduces the statistical error on  $S$  to about 0.04. Also the incorporaton of biased lifetime events, will increase the data volume of about 20%. Furthermore the uncertainty of the flavour tagging, which dominates the systematic uncertainty on  $S$ , will then be greatly reduced.

## Uniformity of $U$

The probability that an event lies within distance  $R$  from event  $i$  is given by

$$\int_{|\vec{x}-\vec{x}_i|<R} \mathcal{P}(\vec{x})d\vec{x}.$$

The probability that none of the other  $n - 1$  events lie closer is

$$\Pr[R^{nn} \geq R] = \left(1 - \int_{|\vec{x}-\vec{x}_i|<R} \mathcal{P}(\vec{x})d\vec{x}\right)^{n-1}.$$

The function

$$y(R) \equiv \int_{|\vec{x}-\vec{x}_i|<R} \mathcal{P}(\vec{x})d\vec{x}$$

is monotonically non-decreasing with  $R$ . Thus we can write

$$\Pr[R^{nn} \geq R] = \Pr[y(R^{nn}) \geq y(R)] = (1 - y)^n$$

making the two substitutions  $\ln U_i = -ny(R^{nn})$  and  $\ln z = -ny(R)$  yields

$$\Pr[U_i \leq z] = \left(1 + \frac{1}{n} \ln z\right)^{n-1}.$$

The pdf for  $U$  is thus given by

$$\mathcal{U}(z) = \frac{d}{dz}\Pr[U_i \leq z] = \frac{n-1}{nz} \left(1 + \frac{1}{n} \ln z\right)^{n-2} \approx 1$$

for  $e^{-n} < z \leq 1$ .



APPENDIX **B**

**Pull Distributions**

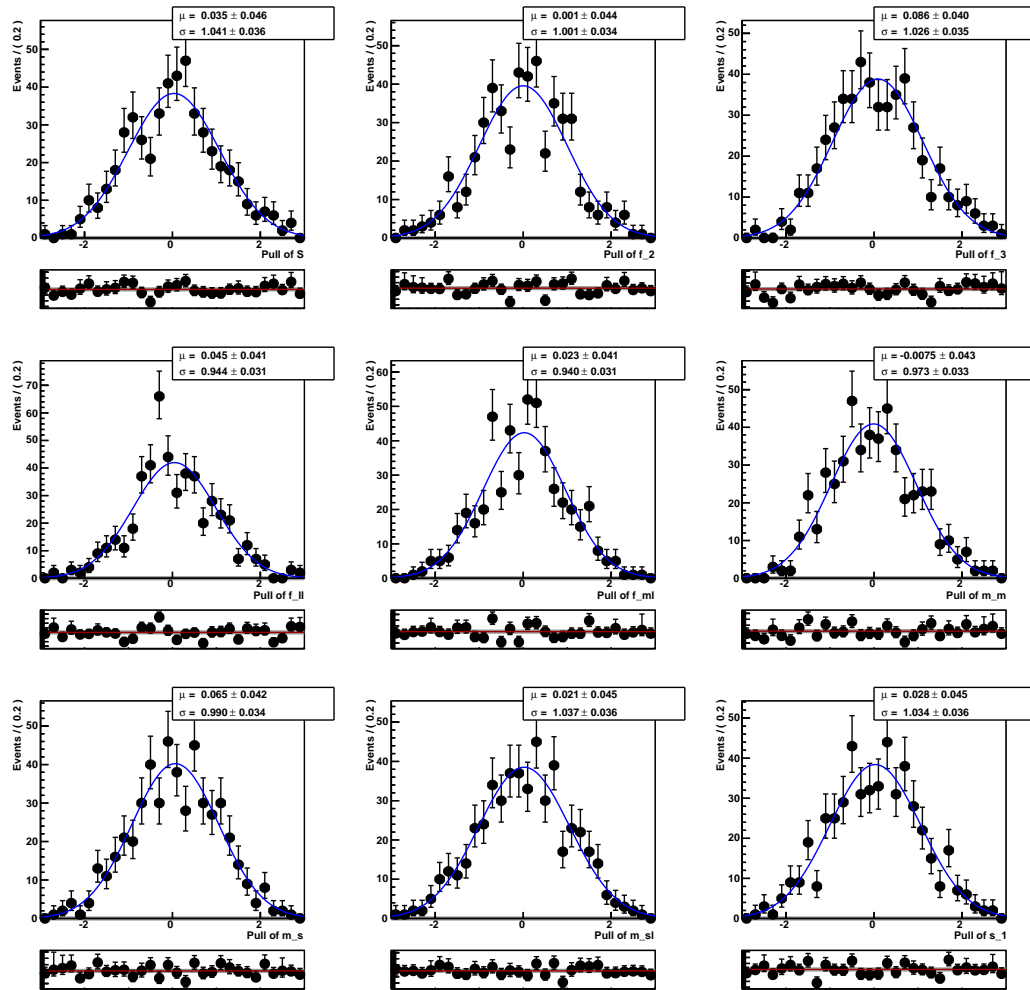


Figure B.1: The pull distributions of the fitted parameters.

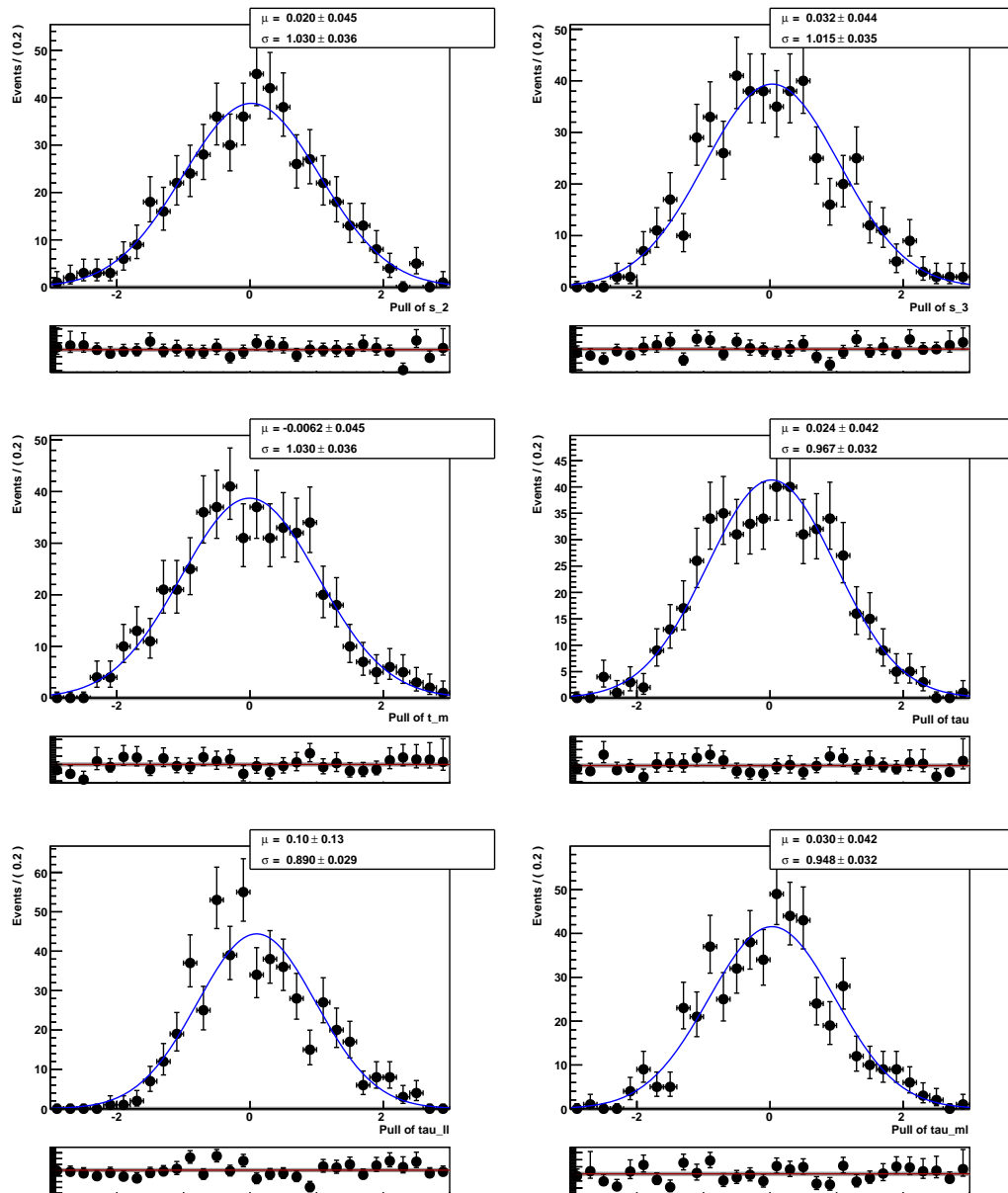


Figure B.2: The pull distributions of the fitted parameters.

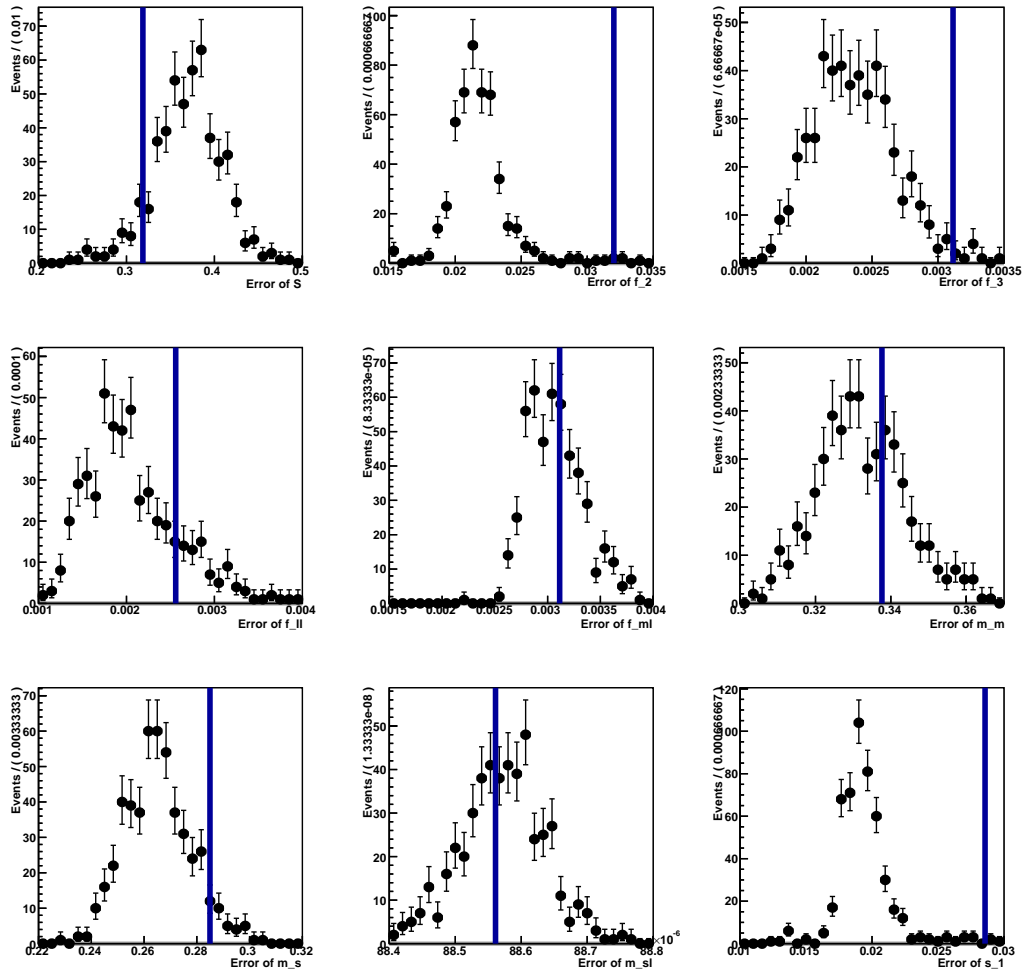


Figure B.3: The error distributions of the fitted parameters.

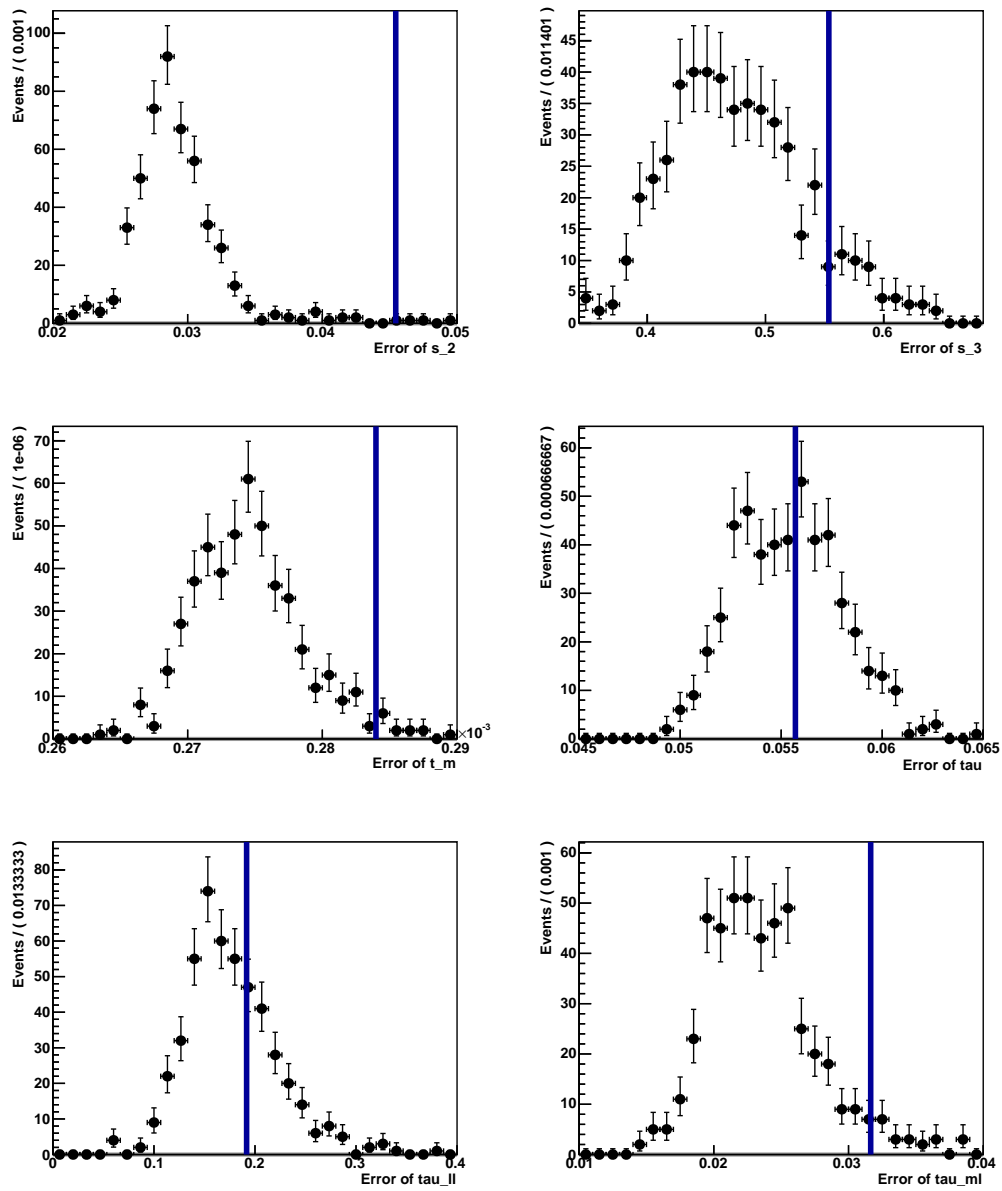
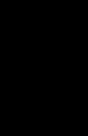


Figure B.4: The error distributions of the fitted parameters.



APPENDIX

C



# Resolution model dependencies

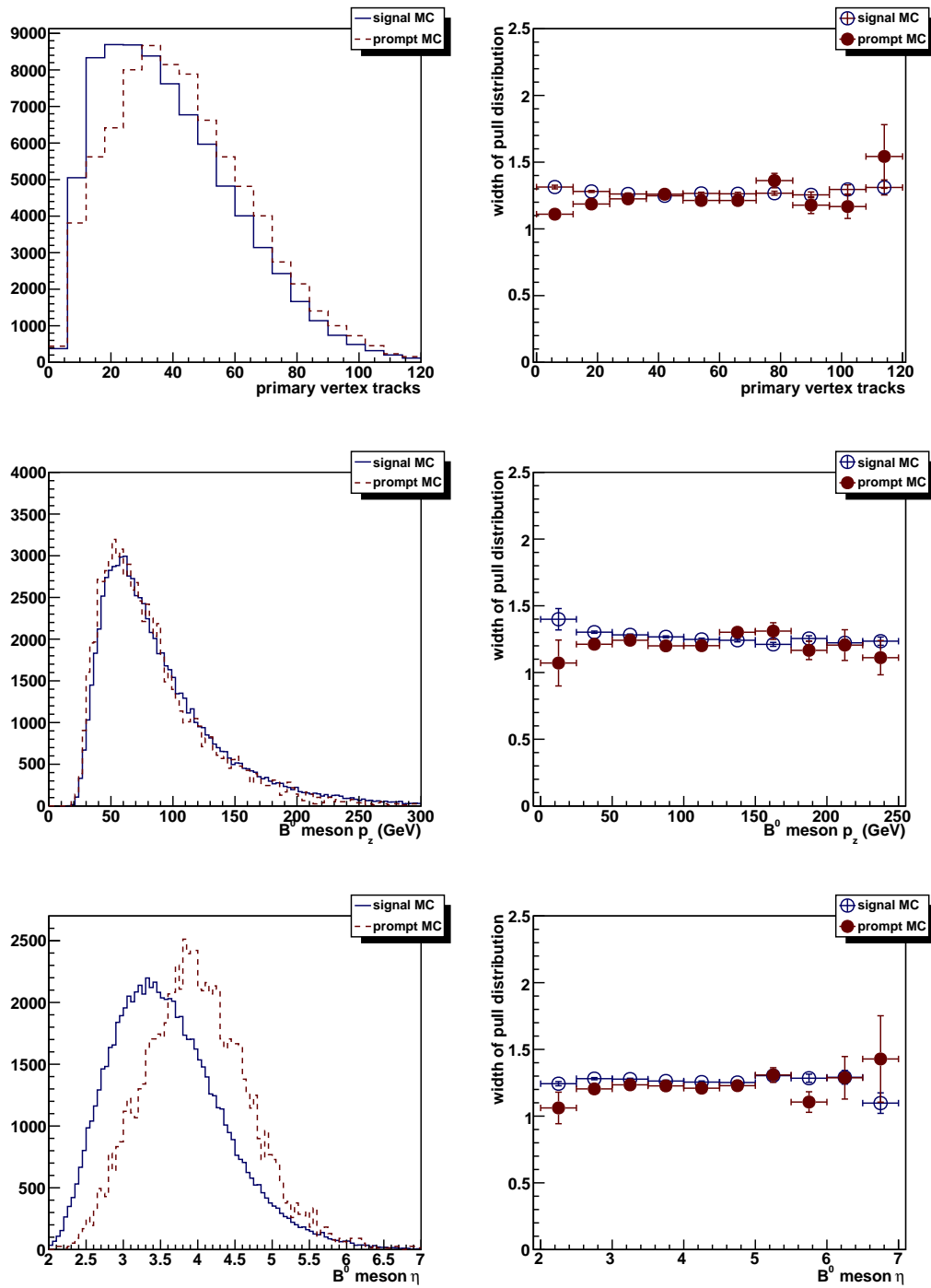


Figure C.1: The resolution dependence of several parameters

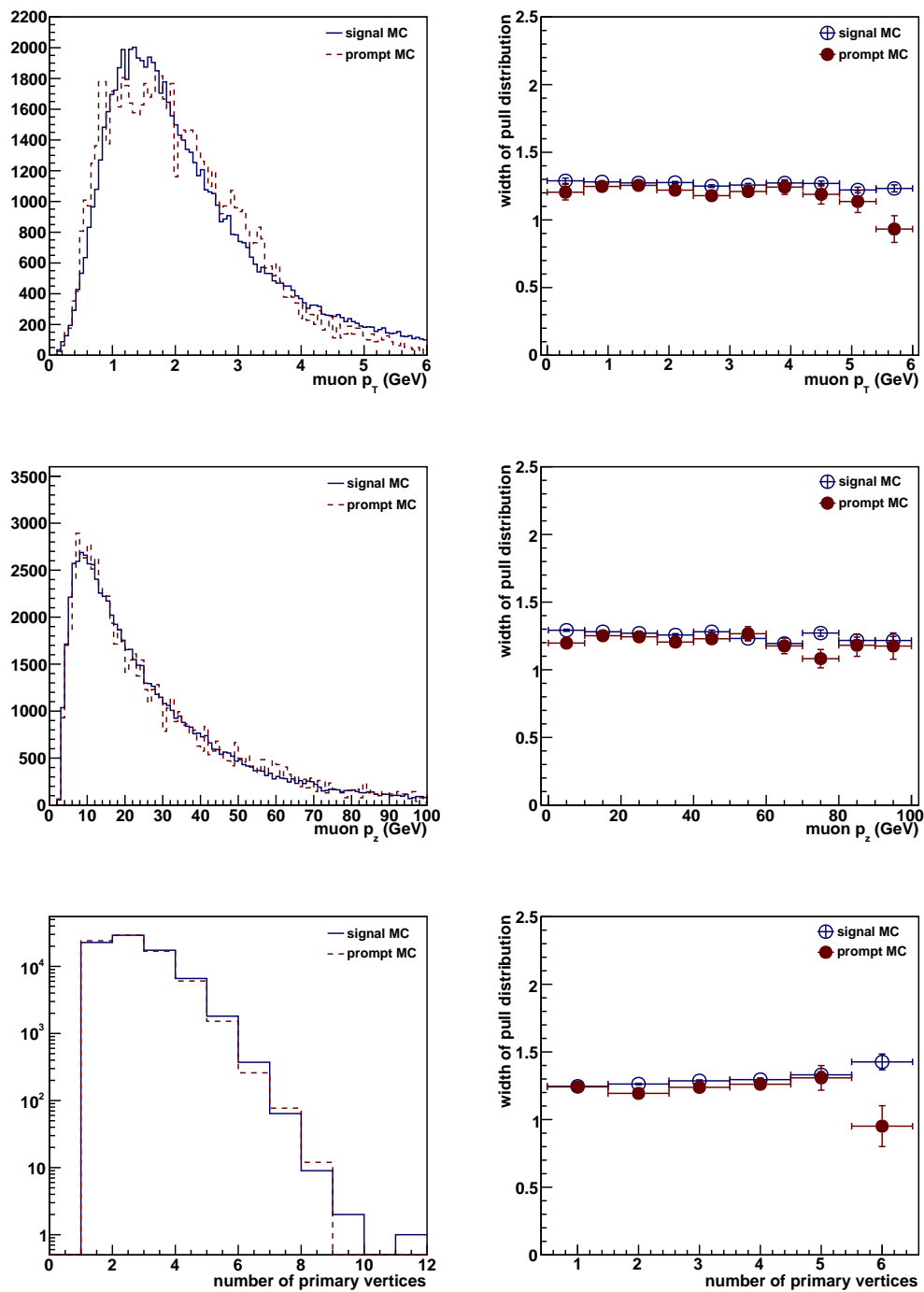
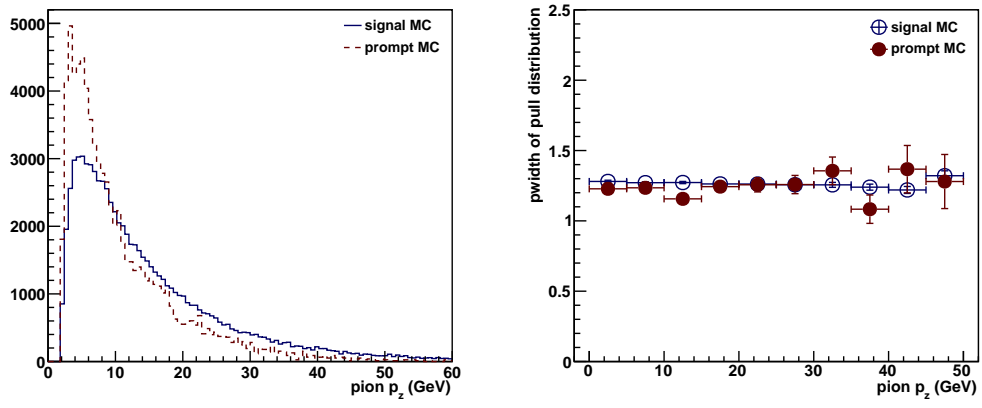


Figure C.2: The resolution dependence of several parameters

Figure C.3: The resolution dependence of the pion  $p_z$

# Bibliography

- [1] *Babar Physics book*  
P.F. Harrison and H.R. Quin (Editors)  
SLAC-R-504, October 1998.
- [2] *The LHCb Detector at the LHC*  
LHCb Collaboration  
JINST 3 (2008) S08005.
- [3] *Optimization and Calibration of the Flavour Tagging performance using 2010 data.*  
T.Brambach et. al.  
LHCb-ANA-2011-003.
- [4] *Measurement of CP violation in the time-dependent analysis of  $B^0 \rightarrow J/\psi K_S$  decays with the 2010 data.*  
T. Brambach et. al.  
LHCb-ANA-2011-004.
- [5] *2011 Review of Particle Physics.*  
K. Nakamura et al. (Particle Data Group)  
J. Phys. G 37, 075021 (2010)
- [6] *Quark Mixing, CP Violation and Rare Decays After the Top Quark Discovery.*  
Andrzej J. Buras and Robert Fleischer  
TUM-HEP-275/97
- [7] *Measurement of Time-Dependent CP Asymmetry in  $B^0 \rightarrow c\bar{c}K^{(*)0}$  Decays*  
B. Aubert et. al. (BABAR Collaboration)  
Phys. Rev. D79, 072009 (2009)
- [8] <http://belle.kek.jp/belle/talks/EPS11/higuchi.pdf>
- [9] *GAUDI - A software architecture and framework for building HEP data processing applications*  
G. Barrand et al.,

- Comput. Phys. Commun. 140 (2001) 45.
- [10] *PYTHIA 6.4 Physics and Manual*.  
Torbjorn Sjostrand, Stephen Mrenna, Peter Z. Skands (Fermilab).  
FERMILAB-PUB-06-052-CD-T, LU-TP-06-13, Mar 2006
- [11] *EvtGen: A Monte Carlo Generator for B-Physics*.  
Anders Ryd et. al.  
EVTGEN-V00-11-07, May 2005
- [12] *Geant4: A simulation toolkit*  
S. Agostinelli et al. (GEANT4 Collaboration)  
Nucl.Instrum. Meth. A506 (2003) 250.
- [13] *Boole: The LHCb digitization program*  
<http://lhcb-release-area.web.cern.ch/LHCb-release-area/DOC/boole/>  
M. Cattaneo et. al., 2004.
- [14] *Introduction to Elementary Particles*  
D. Griffiths
- [15] *Predictions of selected flavour observables within the Standard Model*  
J. Charles et al.  
Phys.Rev.D84:033005, 2011